

THE MASS DISTRIBUTION AND LIFETIME OF PRESTELLAR CORES IN PERSEUS, SERPENS, AND OPHIUCHUS

MELISSA L. ENOCH^{1,3}, NEAL J. EVANS II², ANNEILA I. SARGENT³, JASON GLENN⁴, ERIK ROSOLOWSKY^{5,6}, AND PHILIP MYERS⁶

Draft version October 29, 2018

ABSTRACT

We present an unbiased census of starless cores in Perseus, Serpens, and Ophiuchus, assembled by comparing large-scale Bolocam 1.1 mm continuum emission maps with *Spitzer* c2d surveys. We use the c2d catalogs to separate 108 starless from 92 protostellar cores in the 1.1 mm core samples from Enoch et al. (2006), Young et al. (2006), and Enoch et al. (2007). A comparison of these populations reveals the initial conditions of the starless cores. Starless cores in Perseus have similar masses but larger sizes and lower densities on average than protostellar cores, with sizes that suggest density profiles substantially flatter than $\rho \propto r^{-2}$. By contrast, starless cores in Serpens are compact and have lower masses than protostellar cores; future star formation will likely result in lower mass objects than the currently forming protostars. Comparison to dynamical masses estimated from the NH₃ survey of Perseus cores by Rosolowsky et al. (2008) suggests that most of the starless cores are likely to be gravitationally bound, and thus prestellar. The combined prestellar core mass distribution includes 108 cores and has a slope of $\alpha = -2.3 \pm 0.4$ for $M > 0.8 M_{\odot}$. This slope is consistent with recent measurements of the stellar initial mass function, providing further evidence that stellar masses are directly linked to the core formation process. We place a lower limit on the core-to-star efficiency of 25%. There are approximately equal numbers of prestellar and protostellar cores in each cloud, thus the dense prestellar core lifetime must be similar to the lifetime of embedded protostars, or 4.5×10^5 years, with a total uncertainty of a factor of two. Such a short lifetime suggests a dynamic, rather than quasi-static, core evolution scenario, at least at the relatively high mean densities ($n > 2 \times 10^4 \text{ cm}^{-3}$) to which we are sensitive.

Subject headings: stars: formation — ISM: clouds — ISM: individual (Perseus, Serpens, Ophiuchus) — submillimeter — infrared: ISM

1. INTRODUCTION

Dense prestellar cores, from which a new generation of stars will form, represent a very early stage of the low mass star formation process, before collapse results in the formation of a central protostar. The mass and spatial distributions of these prestellar cores retain imprints of their formation process, and their lifetime is extremely sensitive to the dominant physics controlling their formation. It is well established that most of the star formation in our Galaxy occurs in clusters and groups within large molecular clouds (e.g., Lada & Lada 2003, and references therein). Molecular clouds are known to be turbulent, with supersonic line-widths (e.g., McKee & Zweibel 1992), and to have complex magnetic fields that are likely important to the cloud physics (e.g., Crutcher 1999). Understanding the properties of prestellar cores on molecular cloud scales, and how they vary with environment, provides insight into the global physical processes con-

trolling star formation in molecular clouds.

For example, in the classic paradigm of magnetically dominated star formation (Shu et al. 1987), the collapse of cores occurs very slowly via ambipolar diffusion and starless cores should be long lived, with lifetimes of order $t_{\text{AD}} \sim 10t_{\text{ff}}$ (Nakano 1998), where t_{ff} is the free-fall timescale ($t_{\text{ff}} \sim 10^5 \text{ yr}$ for $n \sim 10^5 \text{ cm}^{-3}$, where t_{ff} depends on the mean core density n : $t_{\text{ff}} \propto n^{-0.5}$). Alternatively, if molecular cloud evolution is driven primarily by turbulence, over-dense cores should collapse quickly, on approximately a dynamical timescale, $1 - 2t_{\text{ff}}$ (Ballesteros-Paredes et al. 2003; Mac Low & Klessen 2004). Thus, the lifetime of prestellar cores should be a strong discriminator of core formation mechanisms. Published measurements of the prestellar core lifetime vary by two orders of magnitude, however, from a few times 10^5 years to 10^7 years (see Ward-Thompson et al. 2007 and references therein).

While the properties of star-forming cores depend strongly on the physical processes leading to their formation, core initial conditions in turn help to determine the evolution of newly formed protostars. One of the most important diagnostics of initial conditions is the mass distribution of prestellar cores. In addition to being a testable prediction of core formation models, a comparison of the core mass distribution (CMD) to the stellar initial mass function (IMF) may reveal what process is responsible for determining stellar masses (e.g., Meyer et al. 2000).

Electronic address: MLE: menoch@astro.berkeley.edu

¹ Department of Astronomy, Univ. of California, Berkeley, CA, 94720

² The University of Texas at Austin, Astronomy Department, 1 University Station C1400, Austin, TX, 78712-0259

³ Division of Physics, Mathematics & Astronomy, California Institute of Technology, Pasadena, CA 91125

⁴ Center for Astrophysics and Space Astronomy, 389-UCB, University of Colorado, Boulder, CO 80309

⁵ University of British Columbia, Okanagan, 3333 University Way, Kelowna BC V1V 1V7 Canada

⁶ Harvard-Smithsonian Center for Astrophysics, 60 Garden St., Cambridge, MA 02138

A number of recent studies have found observational evidence that the shape of the IMF is directly tied to the core fragmentation process (Testi & Sargent 1998; Motte et al. 1998; Onishi et al. 2002). Alves et al. (2007) find a turnover in the CMD of the Pipe Nebula at $M \sim 3 \times$ the turnover in the Trapezium IMF (Muench et al. 2002), and suggest that the stellar IMF is a direct product of the CMD, with a uniform core-to-star efficiency of $30\% \pm 10\%$. The mean particle densities of the extinction-identified cores in Pipe Nebula study ($5 \times 10^3 - 2 \times 10^4 \text{ cm}^{-3}$) are lower than those of typical cores traced by dust emission ($2 \times 10^4 - 10^6 \text{ cm}^{-3}$; Enoch et al. 2007), however, and the cores may not be truly prestellar. In Orion, Nutter & Ward-Thompson (2007) find a turnover in the CMD of starless SCUBA $850 \mu\text{m}$ cores at $\sim 1.3 M_{\odot}$. Those authors relate this turnover to a down-turn in the Kroupa (2002) IMF at $\sim 0.1 M_{\odot}$, and infer a much lower core-to-star efficiency of 6%.

Large samples of prestellar cores are important for further addressing these problems, as is a more reliable separation of prestellar, protostellar, and unbound starless cores. We follow Di Francesco et al. (2007) in defining starless cores as low mass dense cores without a compact internal luminosity source, and prestellar cores, at least conceptually, as starless cores that are gravitationally bound and will form stars in the future. For millimeter cores containing a compact luminous internal source (i.e., an embedded protostar) we follow Di Francesco et al. (2007) in terming these protostellar cores, regardless of whether the final object will be stellar or sub-stellar in nature. Unlike protostellar cores, which are internally heated by the embedded source as well as externally by the interstellar radiation field (ISRF), starless cores are heated only externally by the ISRF, with decreasing temperatures toward the core center (e.g., Evans et al. 2001).

Molecular line or extinction surveys often trace relatively low density material ($10^3 - 10^4 \text{ cm}^{-3}$), leaving the possibility that such cores may never collapse to form stars. In addition, most previous studies base the identification of protostellar versus starless cores on near-infrared data, which is not sensitive to the most embedded protostars, or on low resolution and poor sensitivity IRAS maps. The first issue can be remedied by using millimeter or submillimeter surveys; (sub)mm emission traces dense ($n \gtrsim 2 \times 10^4 \text{ cm}^{-3}$; Ward-Thompson et al. 1994; Enoch et al. 2007) material, and detection at (sub)mm wavelengths tends to correlate with other indications of a prestellar nature, such as inward motions (Gregersen & Evans 2000). *Spitzer* provides significant progress on the second issue, with substantially superior resolution and sensitivity ($0.01 L_{\odot}$ at 260 pc; Harvey et al. 2007a) compared to IRAS, making the identification of prestellar cores much more secure. Recent examples of identifying starless cores include the studies of Jørgensen et al. (2007) and Hatchell et al. (2007), which utilize SCUBA $850 \mu\text{m}$ surveys and *Spitzer* data to distinguish starless from protostellar cores in the Perseus molecular cloud.

The combination of (sub)mm studies with molecular line observations of dense gas tracers, which yield a gas temperature and line-width, is a powerful method for determining the mechanical balance of starless cores. While our preliminary operational definition of a prestellar core will be a starless core that is detected at submillimeter or millimeter wavelengths, we will examine this issue more closely in § 4. Comparison of our data to molecular line observations, such as the recent GBT NH_3 (2,2) and (1,1) survey of Bolocam cores in Perseus by Rosolowsky et al. (2008) provides a more robust method of estimating whether cores are gravitationally bound.

We have recently completed large continuum surveys at $\lambda = 1.1 \text{ mm}$ of the Perseus, Ophiuchus, and Serpens molecular clouds using Bolocam at the Caltech Submillimeter Observatory (CSO). We mapped 7.5 deg^2 (140 pc^2 at our adopted cloud distance of $d = 250 \text{ pc}$) in Perseus, 10.8 deg^2 (50 pc^2 at $d = 125 \text{ pc}$) in Ophiuchus, and 1.5 deg^2 (30 pc^2 at $d = 260 \text{ pc}$) in Serpens with a resolution of $31''$ (Enoch et al. 2006; Young et al. 2006; Enoch et al. 2007, hereafter Papers I, II, and III, respectively). Millimeter emission traces the properties of starless cores and protostellar envelopes, including core sizes, shapes, masses, densities, and spatial distribution. The 1.1 mm Bolocam surveys are complemented by large *Spitzer* Space Telescope IRAC and MIPS maps of the same clouds from the ‘‘From Molecular Cores to Planet-forming Disks’’ *Spitzer* Legacy program (‘‘Cores to Disks’’ or c2d; Evans et al. 2003). Combining these data sets with the 2MASS survey provides wavelength coverage from $1.25 - 160 \mu\text{m}$, and enables us to reliably differentiate starless cores from those that have already formed embedded protostars. The *Spitzer* c2d IRAC and MIPS surveys of each cloud are described in detail in Jørgensen et al. (2006), Harvey et al. (2006), Rebull et al. (2007), Padgett et al. (2007), and Harvey et al. (2007a).

In Paper III, we looked at how the global molecular cloud environment influences the properties of star-forming cores, by comparing the 1.1 mm core populations in Perseus, Serpens, and Ophiuchus. In a companion paper to this work (Enoch et al. 2008, in prep), we use the comparison of 1.1 mm and *Spitzer* data to study the properties of embedded protostars. In particular, we examine the bolometric temperatures and luminosities of Class 0 and Class I protostars in Perseus, Serpens, and Ophiuchus, the lifetime of the Class 0 phase, and accretion rates and history for the early protostellar phases. Here we use the combination of Bolocam 1.1 mm and *Spitzer* c2d surveys to probe the initial conditions of star formation on molecular cloud scales, and how the properties of starless cores differ from cores that have already formed protostars.

In §2 we describe the identification of protostellar cores, including the combination of 1.1 mm and *Spitzer* infrared (IR) data (§ 2.1), identification of candidate protostars based on their mid- and far-infrared properties (§2.2), and the basis on which we determine association between 1.1 mm cores and candidate protostars (§ 2.3). The resulting starless and protostellar 1.1 mm core populations for each cloud are compared in §3, including core sizes and shapes (§3.1), masses and densities (§3.2), distribution in mass versus size (§3.3), relationship to cloud

⁷ The mean particle density of Bolocam cores is given by $n = 3M/(4\pi R\mu m_H)$, where M is the core mass, R the radius, $\mu = 2.33$ is the mean molecular weight per particle, and m_H the mass of Hydrogen.

column density (§3.4), and spatial clustering (§3.5). We calculate the dynamical mass of starless cores in Perseus using NH_3 observations to determine if the cores are truly prestellar (§ 4). We combine the three clouds to produce the prestellar core mass distribution (CMD), which is discussed in relation to the stellar initial mass function in §5. Finally, in § 6 we estimate the lifetime of the dense prestellar core phase and discuss implications for star formation theory.

2. SEPARATING STARLESS AND PROTOSTELLAR CORES

To study the initial conditions of star formation as traced by prestellar cores, we first must differentiate cores without an internal source of luminosity (starless cores) from those with an embedded self-luminous source (protostellar cores). Protostellar cores will have lost some mass due to accretion onto the embedded protostar, and may be otherwise altered, so that they are no longer representative of core initial conditions. Starless and protostellar cores can be differentiated using the *Spitzer* c2d surveys, by identifying infrared sources that may be associated with a given core. Such candidate protostars are typically visible as point-like objects in the near- to mid-infrared data. In the following sections we describe the merging of the millimeter and infrared data and the criteria used to determine which cores are protostellar.

2.1. Combining Bolocam and Spitzer c2d Data

Spitzer IRAC and MIPS maps from the c2d Legacy program cover nearly the same area as our Bolocam 1.1 mm maps of Perseus, Serpens, and Ophiuchus. Both Bolocam and *Spitzer* maps were designed to cover down to a visual extinction of $A_V \gtrsim 2$ mag in Perseus, $A_V \gtrsim 3$ mag in Ophiuchus, and $A_V \gtrsim 6$ mag in Serpens (Evans et al. 2003). The actual overlap in area between Bolocam and IRAC maps is shown in Figure 1 of Papers I, II and III for Perseus, Ophiuchus, and Serpens, respectively. Catalogs listing c2d *Spitzer* fluxes of all detected sources in each of the three clouds, as well as near-infrared fluxes for sources that also appear in the 2MASS catalogs, are available through the *Spitzer* database (Evans et al. 2007). Thus, we have wavelength coverage from $\lambda = 1.25$ to 1100 μm , utilizing 2MASS ($\lambda = 1.25, 1.65, 2.17 \mu\text{m}$), IRAC ($\lambda = 3.6, 4.5, 5.8, 8.0 \mu\text{m}$), MIPS ($\lambda = 24, 70, 160 \mu\text{m}$), and Bolocam ($\lambda = 1.1 \text{ mm}$) data. Note that 160 μm flux measurements are not included in the c2d delivery catalogs due to substantial uncertainties and incompleteness, but are utilized here and in Enoch et al. (2008, in prep.) when possible.

Basic data papers describe the processing and analysis of the *Spitzer* IRAC and MIPS maps of Perseus, Serpens, and Ophiuchus, and present general properties of the sources in each cloud such as color-color and color-magnitude diagrams (Jørgensen et al. 2006; Harvey et al. 2006; Rebull et al. 2007; Harvey et al. 2007a). In addition, the young stellar object (YSO) population in Serpens is discussed in detail by Harvey et al. (2007b). Here we are most interested in very red sources that are likely to be embedded in the millimeter cores detected with Bolocam. For the following we will use the term “candidate protostar” in general to encompass candidate Class 0 and Class I objects (André et al. 1993; Lada & Wilking 1984), although more evolved sources

may be included in this sample as well. A more detailed study of the properties of the candidate protostars themselves is carried out in a companion paper (Enoch et al., in prep).

In Figure 1 we show the result of combining *Spitzer* and Bolocam data for a few cores in each cloud. Three-color (8, 24, 160 μm) *Spitzer* images are overlaid with 1.1 mm Bolocam contours, and symbols mark the positions of all identified 1.1 mm starless cores (“x”s) and protostellar cores (squares). Bolocam IDs of the central sources, from Table 1 of Papers I–III, are given at the top of each image. Red 160 μm images are often affected by saturation, pixel artifacts (bright pixels), and incomplete coverage. Saturation by bright sources affects many pixels in a given scan; this and incomplete sampling accounts for the striped appearance of the red images, particularly in Ophiuchus.

Note the lack of infrared point sources near the center of the starless 1.1 mm cores, whereas protostellar 1.1 mm cores are clearly associated with one or more *Spitzer* sources. Apart from these common traits, both starless and protostellar cores display a wide range of properties. They may be isolated single sources (e.g. Per-Bolo 62, Oph-Bolo 42), associated with filaments or groups (Per-Bolo 74, Ser-Bolo 20), or found near very bright protostars (Per-Bolo 57). Although most of the starless cores are extended, some are quite compact (e.g., Per-Bolo 57), barely resolved by the 31” Bolocam beam. Some starless cores are distinguished in the *Spitzer* bands by their bright 160 μm emission. Per-Bolo 62 is not detectable at 24 or 70 μm , but emerges as a diffuse source at 160 μm , indicating a cold, extended core that closely mirrors 1.1 mm contours. Other starless cores stand out as dark “shadows” in the shorter wavelength bands. Ser-Bolo 18 and Oph-Bolo 26 are two examples of such cores; the dark shadows against bright 8 and 24 μm emission are suggestive of dense cores obscuring background nebular emission. Again, contours at 1.1 mm closely trace the *Spitzer* short-wavelength shadows.

Although the sky coverage of the IRAC, MIPS and Bolocam maps overlaps nearly perfectly for our purposes, there is a small portion of the Serpens 1.1 mm map that is not covered by the 70 μm map. In addition, the 160 μm maps are often saturated near bright sources and in regions of bright extended emission, such as near bright clusters of sources.

2.2. Identifying Candidate Protostars

The identification of candidate protostars is discussed in more detail in Enoch et al. (2008, in prep); here we briefly describe the sample used to identify protostellar cores. The first criteria used to select candidate protostars from the c2d source catalogs is based on the source “class.” All sources in the c2d database are assigned a class parameter based on colors, magnitudes, and stellar SED fits, as discussed in the c2d Delivery Document (Evans et al. 2007) and in Harvey et al. (2007a). Class parameters include “star”, “star+disk”, “YSOc” (young stellar object candidate), “red”, “rising”, “Galc” (galaxy candidate), etc. Protostar candidates will generally be a subset of YSOc sources, but some of the most embedded may also be assigned to the “red” class if they are not detected in all four IRAC bands.

A preliminary sample is formed from sources classi-

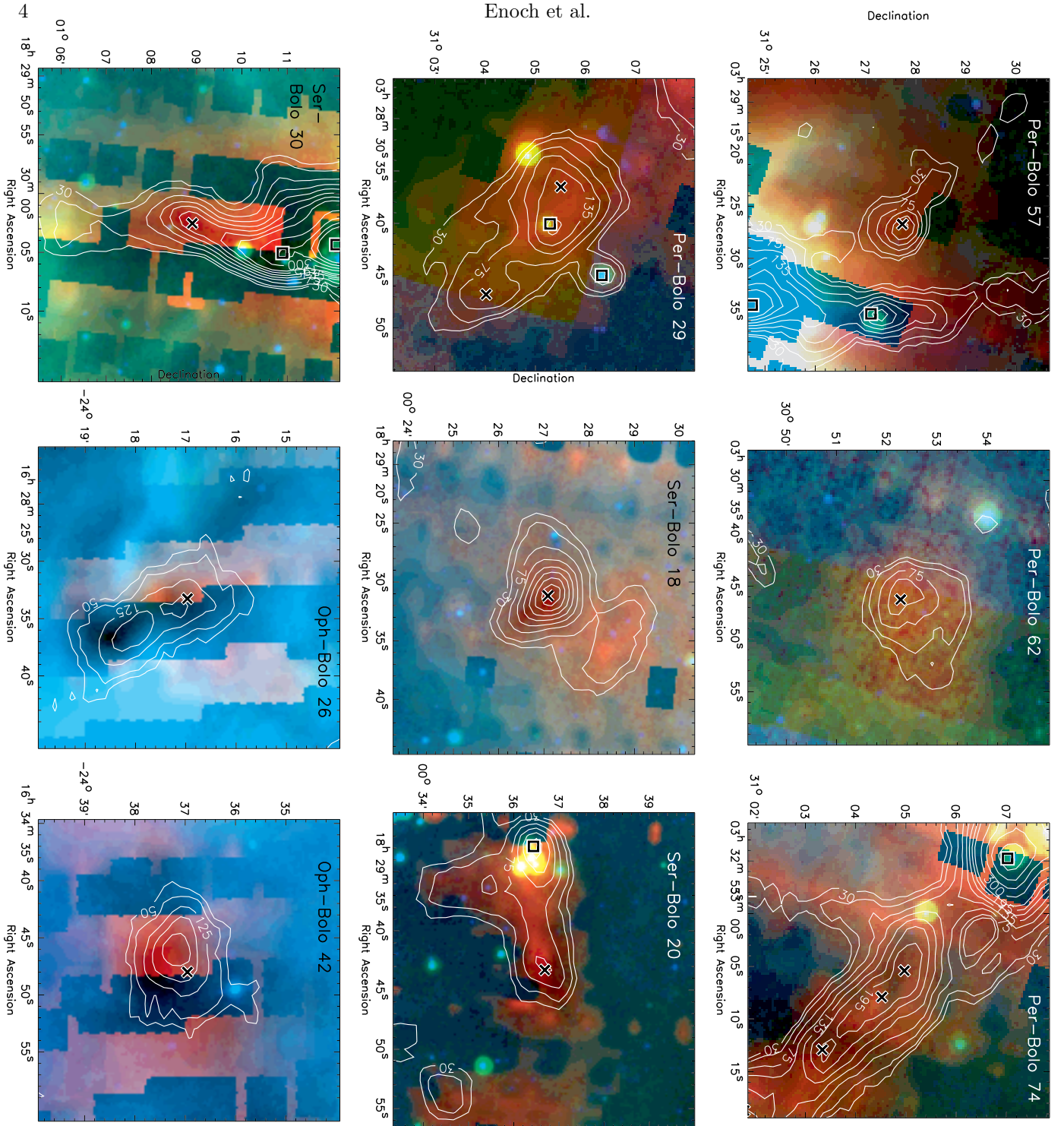


FIG. 1.— Three color *Spitzer* images (8.0, 24, 160 μm) of selected starless and protostellar cores in Perseus, Serpens, and Ophiuchus. Bolocam 1.1 mm contours are overlaid at intervals of 2, 3, 5, ...15, 20...35 σ , where 1σ is the mean rms noise in each 1.1 mm Bolocam map (15 mJy in Perseus, 10 mJy in Serpens, and 25 mJy in Ophiuchus). Positions of starless cores are indicated by an “x”, protostellar cores by a square, and the Bolocam ID of the centered core is given. Note the lack of infrared point sources near the starless core positions. Starless cores are most notable in the infrared by their extended 160 μm emission or dark shadows at shorter wavelengths, while protostellar cores are clearly associated with *Spitzer* point sources. Saturation, image artifacts, and incomplete sampling causes the striped appearance of some of the red 160 μm images.

fied as “YSOc” or “red.” We impose a flux limit at $\lambda = 24\mu\text{m}$ of $S_{24\mu\text{m}} \geq 3 \text{ mJy}$ ⁸, high enough to eliminate most extragalactic interlopers and sources with SEDs

that are clearly inconsistent with an embedded nature (e.g., sources with $S_{24\mu\text{m}} < S_{8\mu\text{m}}$), but low enough to

0.7 mJy limit imposed by Harvey et al. (2007b), together with several other criteria, to help eliminate galaxies.

⁸ Note that this limit is considerably higher than the $S_{24\mu\text{m}} \gtrsim$

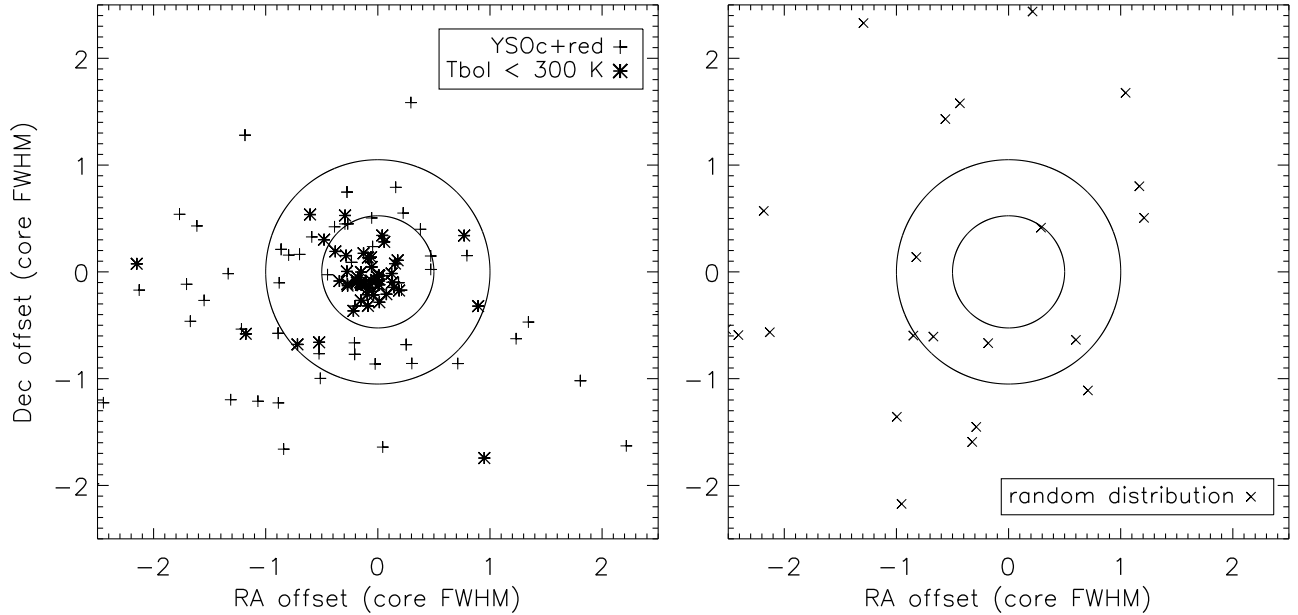


FIG. 2.— *Left*: Distribution of the positional offset from each protostar candidate in Perseus to the nearest 1.1 mm core centroid. Distances are in units of the core FWHM size (θ_{1mm}), and circles enclose sources within 0.5 and 1.0 θ_{1mm} of a core position. Pointing errors in the Bolocam maps are typically $10''$ or less. Protostar candidates include all “YSOc”, “red” and $70\ \mu\text{m}$ sources, while candidates with bolometric temperatures $T_{bol} < 300$ K (Enoch et al. 2008, in prep) are shown in bold. These cold objects, which are most likely to be most embedded, are primarily located within 1.0 θ_{1mm} of a core centroid. *Right*: Expected distribution if the IR sources were distributed randomly over the Bolocam map area (i.e. if they were not spatially correlated with the cores). Our definition that a given 1.1 mm core is protostellar if there is a candidate protostar within 1.0 θ_{1mm} of the core position will result in a few false associations in each cloud.

include most deeply embedded known protostars. In addition, we include any $70\ \mu\text{m}$ point sources that are not classified as galaxy candidates (“Galc”). In each cloud, a few known deeply embedded sources that have strong $70\ \mu\text{m}$ emission but very weak $24\ \mu\text{m}$ emission (e.g., HH211 in Perseus) are recovered by this last criteria, as are a few very bright sources that are saturated at $24\ \mu\text{m}$ (these are often classified as “rising”). The *Spitzer* c2d surveys are complete to young objects with luminosities as low as $0.05L_{\odot}$ (Dunham et al. 2008, in prep.; Harvey et al. 2007a), and we are unlikely to be missing any protostellar sources down to this level (Enoch et al. 2008, in prep.; Dunham et al. 2008, in prep.).

2.3. Determining association between cores and candidate protostars

We next determine which of the 1.1 mm cores are associated with a candidate protostar. The positional offset from each candidate protostar to the nearest 1.1 mm core centroid position, in units of the core full-width at half-maximum (FWHM) size, is plotted in Figure 2 (left). Note that this analysis is similar to Figure 2 of Jørgensen et al. (2007). Large circles enclose candidate protostars that are located within $0.5 \times \theta_{1mm}$ and $1.0 \times \theta_{1mm}$ of a 1.1 mm core position, where θ_{1mm} is the angular FWHM size of a given core (the measurement of core sizes is described in § 3.1). Protostellar sources with bolometric temperature $T_{bol} < 300$ K (Enoch et al. 2008, in prep.) are indicated by bold symbols. In general, the coldest objects, those expected to be embedded within millimeter cores, are located within $1.0 \times \theta_{1mm}$ of a 1.1 mm core position. Thus we define protostellar cores to be those cores which have a candidate protostar

located within $1.0 \times \theta_{1mm}$ of the core center. Note that protostellar cores are defined by any candidate protostar within $1.0 \times \theta_{1mm}$, not only those with $T_{bol} < 300$ K.

The right panel of Figure 2 demonstrates what we would expect if the same sample of *Spitzer* sources was distributed randomly over the Bolocam map area. Although there are approximately the same number of sources in the random sample as in the candidate protostar sample, most do not appear on the plot because they are located much farther than $2 \times \theta_{1mm}$ from the nearest core. There are 5 sources from the random sample located within $1.0 \times \theta_{1mm}$ of a core position; thus we can expect a few false associations between 1.1 mm cores and candidate protostars based on this criteria. Indeed, some associations between cores and *Spitzer* sources are probably just projections on the sky. We are especially skeptical of associations where the 1.1 mm core flux density is much higher than the $70\ \mu\text{m}$ flux. Using $0.5 \times \theta_{1mm}$ would be a more restrictive choice, but might mis-identify some protostellar cores as starless. As we do not want to contaminate our starless core sample with more evolved sources, we adopt the more conservative criteria. Thus the number of starless cores in each cloud is likely a lower limit to the true value; using $0.5 \times \theta_{1mm}$ would result in 3 more starless cores in Perseus, 2 in Serpens, and 4 in Ophiuchus.

3. COMPARING THE STARLESS AND PROTOSTELLAR 1.1 MM CORE POPULATIONS

Tables 4 and 5 list the Bolocam identifications, positions, and peak flux densities (from Papers I–III) of starless and protostellar cores in each cloud. We find a total of 108 starless and 92 protostellar cores in the three cloud sample. Cores are identified based on a peak flux density

at least 5 times the local rms noise level, and positions are determined using a surface brightness-weighted centroid, as described in Paper III. The Bolocam maps of Perseus, Serpens, and Ophiuchus are shown in Figure 3, with the positions of starless and protostellar cores indicated. The average 1σ rms is 15 mJy beam⁻¹ in Perseus, 10 mJy beam⁻¹ in Serpens, and 25 mJy beam⁻¹ in Ophiuchus.

General core statistics, including the number of starless (N_{SL}) and protostellar (N_{PS}) cores in each cloud, as well as the ratio $N_{\text{SL}}/N_{\text{PS}}$, are given in Table 1. Note that the number of starless and protostellar cores are approximately equal in each cloud ($N_{\text{SL}}/N_{\text{PS}} = 1.2$ in Perseus, 0.8 in Serpens, and 1.4 in Ophiuchus), a fact that will be important for our discussion of the starless core lifetime in §6. The last column of Table 1 gives the number of individual 1.1 mm cores that are associated with more than one candidate protostar (each located within $1 \times \theta_{1\text{mm}}$ of the core position). There are 13 such “multiple” protostellar sources in Perseus (24% of the protostellar core sample), 11 in Serpens (55%), and 3 in Ophiuchus (17%). In general there are two or three candidate protostars associated with each “multiple” core, with the exception of one core in Serpens (5 candidate protostars). Throughout this work multiple protostellar cores are treated as single objects.

We now compare the physical properties of the starless and protostellar core populations in each cloud, with two primary goals. Isolating a starless sample allows us to probe the initial conditions of star formation, and differences between the starless and protostellar core samples are indicative of how the formation of a central protostar alters core properties. In the following sections we follow the methodology of Paper III, examining the sizes and shapes of cores, their peak and mean densities, distributions of core mass versus size, spatial clustering properties, and relationship to the surrounding cloud column density.

3.1. Sizes and Shapes

Source angular FWHM sizes (θ_{meas}) are measured by fitting an elliptical Gaussian after masking out nearby sources using a mask radius equal to half the distance to the nearest neighbor (see Paper II). The angular deconvolved core size is the geometric mean of the deconvolved minor and major angular FWHM sizes: $\theta_{\text{dec}} = \sqrt{\theta_{d,\text{maj}} \theta_{d,\text{min}}}$, where $\theta_d = \sqrt{\theta_{\text{meas}}^2 - \theta_{\text{mb}}^2}$ and $\theta_{\text{mb}} = 31''$ is the beam FWHM. Deconvolved sizes for starless and protostellar cores are given in Tables 4 and 5, respectively, and the size distributions are plotted in Figure 4.

As discussed in Paper III, the measured size does not necessarily represent a physical boundary, but rather is a characteristic scale that depends on the linear resolution and intrinsic source density profile. For sources with power law density profiles, which do not have a well defined size, $\theta_{\text{dec}}/\theta_{\text{mb}}$ is independent of distance and simply related to the index of the power law (Young et al. 2003). According to the correlation between $\theta_{\text{dec}}/\theta_{\text{mb}}$ and density power law exponent p found by Young et al. (2003), a mean $\theta_{\text{dec}}/\theta_{\text{mb}}$ value of $50''/31'' = 1.6$ for protostellar cores in Perseus implies an average power law index of $p \sim 1.4$ to 1.5. Many well-known protostellar sources have been found to have envelopes consis-

tent with power law density profiles, as determined by high-resolution imaging combined with radiative transfer modeling. Our inferred average index for Perseus protostellar cores ($p = 1.4 - 1.5$) is consistent with the mean $p \sim 1.6$ from radiative transfer modeling of Class 0 and Class I envelopes (Shirley et al. 2002; Young et al. 2003). For reference, a singular isothermal sphere (SIS) has $p = 2$ ($\theta_{\text{dec}}/\theta_{\text{mb}} \sim 0.9$), and the profile expected for a free-falling envelope is $p = 1.5$ ($\theta_{\text{dec}}/\theta_{\text{mb}} \sim 1.6$) (Shu 1977; Young et al. 2003).

Starless cores in Perseus are larger on average than protostellar cores (Figure 4); the starless distribution is relatively flat, with a few barely resolved cores, and several larger than $3 \theta_{\text{mb}}$. The Student’s T-test confirms that the mean sizes of starless and protostellar cores are significantly different (significance of the T statistic is 2×10^{-5}). A mean $\theta_{\text{dec}}/\theta_{\text{mb}}$ of 2.2 for starless cores in Perseus would imply an extremely shallow mean power law index of $p \sim 1.1$, and the maximum value ($\theta_{\text{dec}}/\theta_{\text{mb}} \sim 3.5$) would correspond to $p < 0.8$. Other flattened profiles, such as the Bonnor-Ebert (BE) sphere (Ebert 1955; Bonnor 1956), could also produce large $\theta_{\text{dec}}/\theta_{\text{mb}}$ values. A BE profile with a central density of 10^5 cm^{-3} and an outer radius of $6 \times 10^4 \text{ AU}$ would correspond to $\theta_{\text{dec}}/\theta_{\text{mb}} = 2.0$ at the distance of Perseus. There is significant observational evidence that many starless cores do indeed look like BE spheres (e.g., Johnstone et al. 2000; Shirley et al. 2000; Alves et al. 2001; Evans et al. 2001). We conclude that very large starless cores are more consistent with BE spheres or other flattened density profiles ($p \lesssim 1$) than with the classical pre-collapse SIS ($p = 2$).⁹

Despite their size differences, there is little difference in the axis ratios of starless and protostellar cores in Perseus (Figure 5). Both populations are slightly elongated on average. The axis ratio is defined at the half-max contour, using deconvolved sizes: $\theta_{d,\text{maj}}/\theta_{d,\text{min}}$. Values for individual cores are given in Tables 4 and 5. Starless and protostellar cores have mean axis ratios of 1.7 ± 0.9 and 1.8 ± 0.9 . Standard deviations quoted here and in the rest of §3 are dispersions in the sample, *not* errors in the mean. Monte Carlo tests (Paper I) indicate that cores with axis ratios less than 1.2 should be considered round.

In contrast to Perseus, starless cores in Serpens are no larger than protostellar cores. Mean values for both ($\theta_{\text{dec}}/\theta_{\text{mb}} \sim 1.5$) correspond to an average power law index of $p = 1.5$, similar to that found for protostellar cores in Perseus, and to typical radiative transfer modeling results for protostellar envelopes. Starless cores in Serpens may be more elongated than protostellar cores (mean axis ratios of 1.7 ± 0.5 and 1.4 ± 0.3 , respectively), but the difference is not statistically significant.

In Ophiuchus there is no measurable difference between the starless and protostellar populations. The starless and protostellar samples have similar mean sizes, and both display a bimodal behavior (Figure 4). The lower peak is similar to the single peak seen in Serpens at $\theta_{\text{dec}} = 1 - 2 \theta_{\text{mb}}$, while the smaller upper peak is at sizes of $\theta_{\text{dec}} = 3 - 4 \theta_{\text{mb}}$, comparable to the largest star-

⁹ As the pressure-truncated boundary radius of the BE solution has not been observationally verified, the resemblance between starless cores and BE profiles is necessarily limited to the region inside the boundary radius. Also note that a sufficiently centrally condensed BE sphere will be indistinguishable from a power law on the scales to which we are sensitive.

TABLE 1
 STATISTICS OF 1.1 MM CORES IN THE THREE CLOUDS

Cloud	N_{total}^1	N_{SL}^2	N_{PS}^3	$N_{\text{SL}}/N_{\text{PS}}$	$N_{\text{PS}} \text{ (mult)}^4$
Perseus	122	67	55	1.2	13
Serpens	35	15	20	0.8	11
Ophiuchus	43	26	17	1.5	3

¹ Total number of identified 1.1 mm cores.

² Number of starless 1.1 mm cores, i.e., cores that do not have a protostar candidate located within $1.0 \times \theta_{1\text{mm}}$ of the core position.

³ Number of protostellar cores.

⁴ Number of protostellar cores that are associated with more than one candidate cold protostar (each within $1.0 \times \theta_{1\text{mm}}$ of the core position).

less cores in Perseus. The mean $\theta_{\text{dec}}/\theta_{\text{mb}}$ for protostellar cores (1.9) corresponds to an average power law index of $p = 1.3$. Both starless and protostellar cores in Ophiuchus appear fairly round, with the mean axis ratios of 1.3 ± 0.2 and 1.4 ± 0.5 , respectively (Figure 5). As discussed in Paper III, larger axis ratios in Perseus and Serpens may be at least partly an effect of the lower linear resolution in those clouds compared to Ophiuchus (e.g. blending).

Were we to calculate linear sizes, cores in Ophiuchus would appear smaller by nearly a factor of two compared to Perseus and Serpens, given the smaller distance to Ophiuchus. This is primarily a systematic effect of the linear resolution, however. In Paper III we found that convolving the Ophiuchus map with a larger beam to match the linear resolution of Perseus and Serpens produced larger linear core sizes by nearly a factor of two, but similar measured $\theta_{\text{dec}}/\theta_{\text{mb}}$ values. Thus we focus here on angular sizes only.

To summarize, protostellar cores in all three clouds have mean sizes consistent with power law density profiles with an average index $p = 1.3 - 1.5$. Starless cores in Perseus are significantly larger on average than protostellar cores, suggestive of BE spheres or other shallow density profiles. Starless cores are quite compact in Serpens, while both starless and protostellar cores in Ophiuchus display a bimodal distribution of sizes, with a few very large cores. The deficit of cores with $\theta_{\text{dec}}/\theta_{\text{mb}} > 2$ in Serpens and Ophiuchus as compared to Perseus may be related to the general lack of isolated sources in those clouds; the measured size of a core is limited by the distance to the nearest neighboring source, so sizes will tend to be smaller in crowded regions (e.g. L 1688 Ophiuchus) than for isolated sources.

3.2. Core Masses and Densities

Core total masses, given in Tables 4 and 5, are calculated from the total 1.1 mm flux, $S_{1.1\text{mm}}$:

$$M = \frac{d^2 S_\nu}{B_\nu(T_D) \kappa_\nu}, \quad (1)$$

where d is the cloud distance, B_ν is the Planck function at dust temperature T_D , and $\kappa_{1.1\text{mm}} = 0.0114 \text{ cm}^2 \text{ g}^{-1}$ is the dust opacity. The total 1.1 mm flux density is integrated in the largest aperture ($30'' - 120''$ diameters in steps of $10''$) that is smaller than the distance to the nearest neighboring source. We assume that the dust emission at $\lambda = 1.1 \text{ mm}$ is optically thin, and that T_D and $\kappa_{1.1\text{mm}}$ are independent of position within a core. The value of $\kappa_{1.1\text{mm}}$ is interpolated from Table 1 column 5

of Ossenkopf & Henning (1994) for dust grains with thin ice mantles, and includes a gas to dust mass ratio of 100. A recent measurement of κ based on near-IR data and $450 \mu\text{m}$ and $850 \mu\text{m}$ SCUBA maps yields $\kappa_{1.1\text{mm}} = 0.0088 \text{ cm}^2 \text{ g}^{-1}$ (Shirley et al. 2007), which would increase our masses by a factor of 1.3.

The value of T_D should depend on whether a core is starless or has an internal source of luminosity, so we assume a slightly higher temperature for protostellar cores ($T_D = 15 \text{ K}$) than for starless cores ($T_D = 10 \text{ K}$). For dense regions without internal heating, the mean temperature is about 10 K , warmer on the outside and colder on the inside (Evans et al. 2001). A recent NH_3 survey of the Bolocam cores in Perseus confirms that the median kinetic temperature of starless cores in Perseus is 10.8 K (see Schnee et al. 2008, in prep, and § 4). Our assumed value of 15 K for protostellar cores is the average isothermal dust temperature found from radiative transfer models of Class 0 and Class I protostars (Shirley et al. 2002; Young et al. 2003). The isothermal dust temperature is the temperature that, when used in an isothermal mass equation (e.g., Eq. 1) yields the same mass as a detailed radiative transfer model including temperature gradients. There is a factor of 1.9 difference in mass between assuming $T_D = 10 \text{ K}$ and 15 K .

Figures 6 and 7 compare the peak and mean densities of starless and protostellar cores in each cloud. We use the peak column density N_{H_2} , calculated from the peak 1.1 mm flux density $S_{1.1\text{mm}}^{\text{beam}}$, as a measure of the peak density:

$$N(\text{H}_2) = \frac{S_\nu^{\text{beam}}}{\Omega_{\text{beam}} \mu_{\text{H}_2} m_{\text{H}} \kappa_\nu B_\nu(T_D)}, \quad (2)$$

with $N(\text{H}_2)/A_V = 0.94 \times 10^{21} \text{ cm}^{-2} \text{ mag}^{-1}$ (Frerking et al. 1982). Here Ω_{beam} is the beam solid angle, m_{H} is the mass of hydrogen, and $\mu_{\text{H}_2} = 2.8$ is the mean molecular weight per H_2 molecule. As discussed in Paper III, the 1.1 mm emission detected by Bolocam traces significantly higher column densities than other tracers such as the reddening of background stars.

Mean particle densities, given in Tables 4 and 5, are calculated within a fixed linear aperture of diameter 10^4 AU :

$$n_{1e4} = \frac{3M_{1e4}}{4\pi(D_{1e4}/2)^3 \mu m_{\text{H}}}, \quad (3)$$

where D_{1e4} is the aperture size (10^4 AU), M_{1e4} is the mass calculated from the 1.1 mm flux within that aperture, and $\mu = 2.33$ is the mean molecular weight per particle. An aperture of 10^4 AU corresponds to approx-

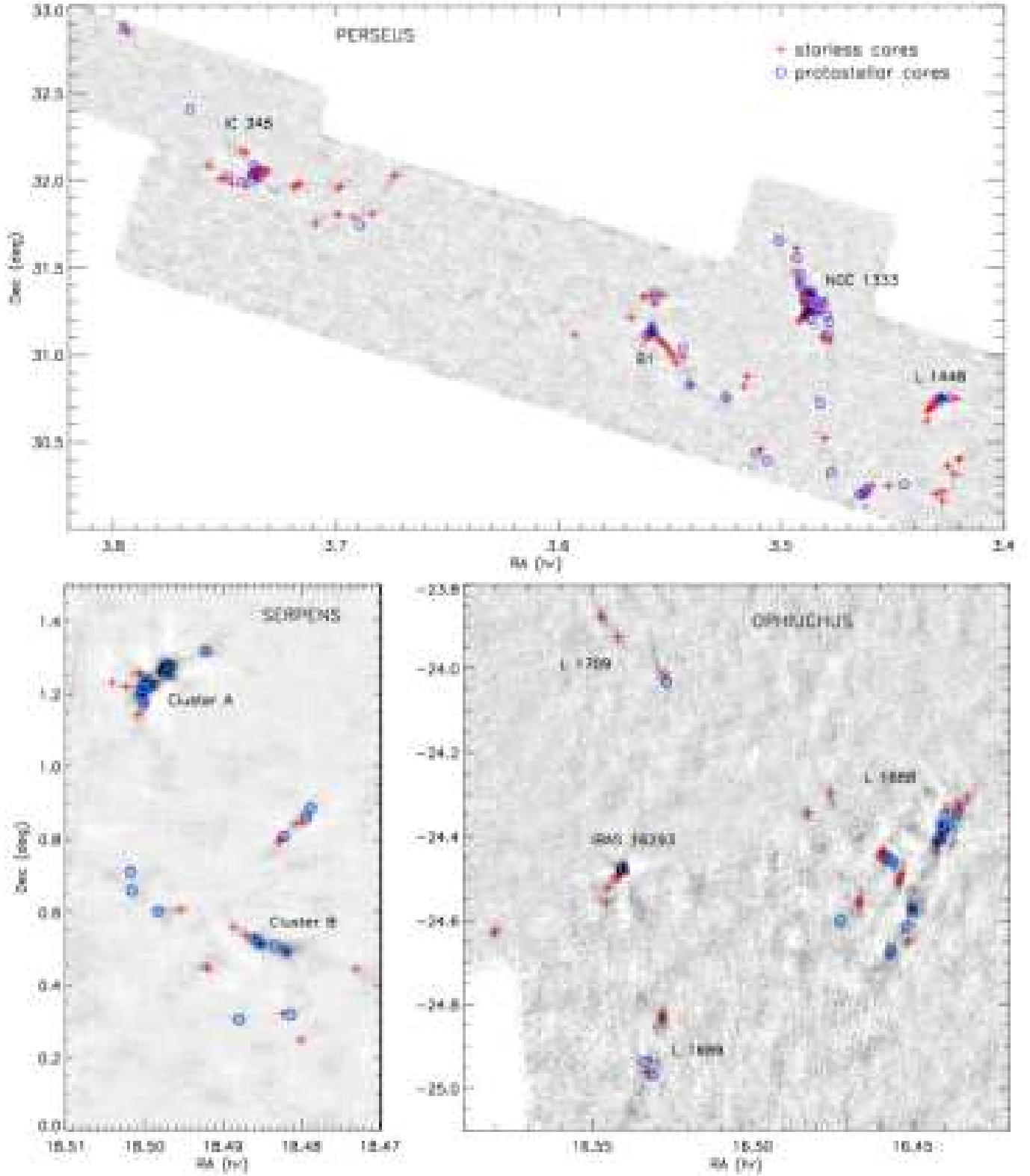


FIG. 3.— Bolocam maps of Perseus, Serpens, and Ophiuchus, with the positions of starless and protostellar cores indicated. Identified cores have peak flux densities of at least 5σ , where σ is the local rms noise level (on average $\sigma = 15 \text{ mJy beam}^{-1}$ in Perseus, 10 mJy beam^{-1} in Serpens, and 25 mJy beam^{-1} in Ophiuchus). Note that due to the large scales, individual structures are difficult to see. Regions of the maps with no detected sources have been trimmed for this figure. Starless and protostellar cores cluster together throughout each cloud, with both populations tending to congregate along filamentary cloud structures. There are a few exceptional regions, however, which are dominated by either starless or protostellar cores (e.g. the B1 Ridge, Serpens Cluster A). imately $40''$ in Perseus and Serpens, and $80''$ in Ophi- uchuus. Note that n_{1e4} does not depend on the core size;

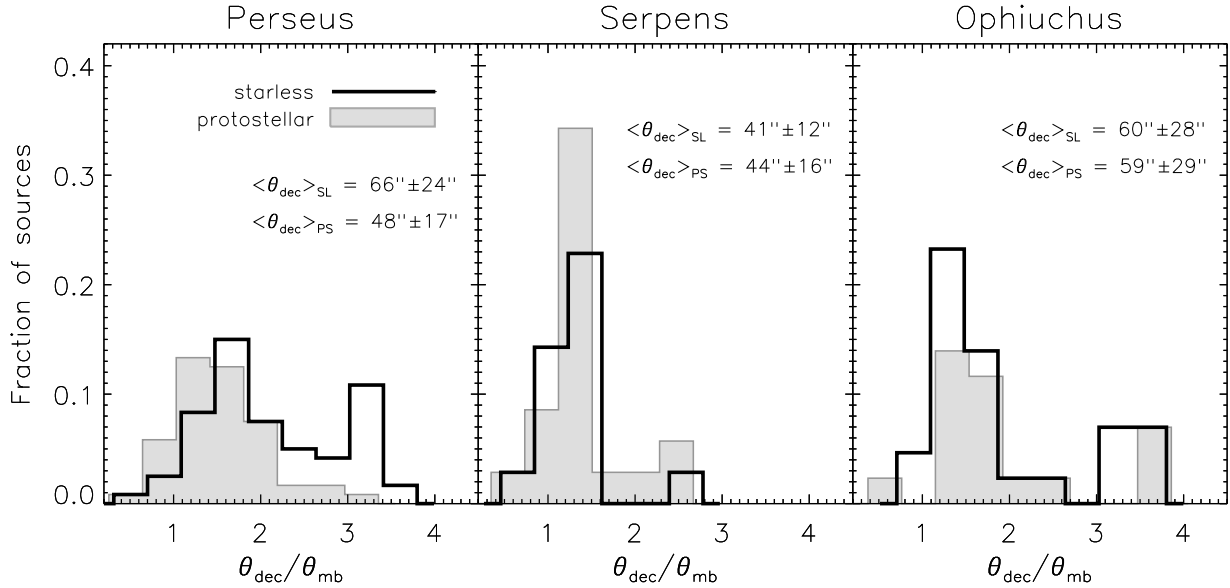


FIG. 4.— Distributions of the angular deconvolved sizes of starless and protostellar cores in the three clouds. The size is given in units of the beam FWHM (θ_{mb}), and the mean of each distribution \pm the dispersion in the sample is listed. Starless cores are larger on average than protostellar cores in Perseus, with a flattened distribution out to $3.5 \theta_{mb}$. In Serpens and Ophiuchus, however, there is little difference between the starless and protostellar distributions, and there are fewer very large cores, particularly in Serpens. The value of θ_{dec}/θ_{mb} can be used to infer the steepness of the source radial density profile (see text and Young et al. 2003).

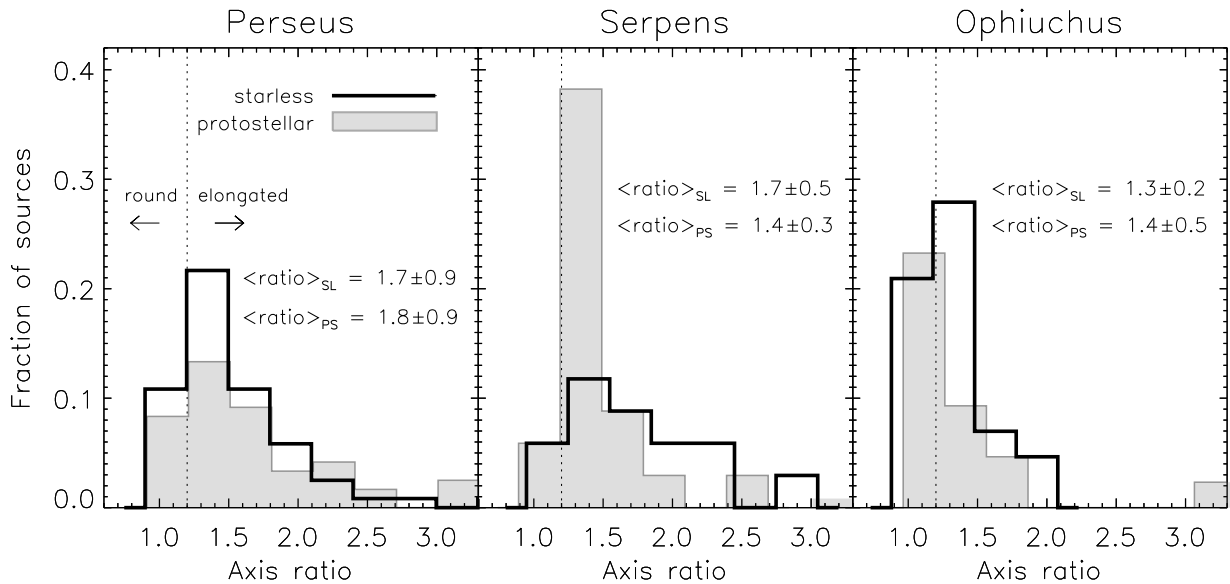


FIG. 5.— Distributions of the axis ratios of starless and protostellar cores. Cores with axis ratios < 1.2 are considered round and those with axis ratios > 1.2 elongated, based on Monte Carlo simulations (Paper I). Only in Serpens, where starless cores tend to be slightly more elongated than protostellar cores, is there a distinguishable difference between the starless and protostellar populations.

while in some cases 10^4 AU may be considerably smaller or larger than the source FWHM, a fixed linear aperture is used here to mitigate the effects of linear resolution, which was found in Paper III to significantly bias the mean density calculated within the FWHM contour.

The average peak column density (N_{H_2}) for starless cores in Perseus is $12 \times 10^{21} \text{ cm}^{-2}$, while the average for protostellar cores is 50% higher, $19 \times 10^{21} \text{ cm}^{-2}$, with a much wider dispersion (the significance of the Student's

T-statistic is 0.03). Similarly, the typical mean density (n_{1e4}) of starless cores ($1.7 \times 10^5 \text{ cm}^{-3}$) is a factor of three smaller than that of protostellar cores ($5.1 \times 10^5 \text{ cm}^{-3}$; Student's T-test significance 6×10^{-5}). The large difference in mean densities is due primarily to the significantly smaller sizes of protostellar cores in Perseus. Recently, Jørgensen et al. (2007) found a similar result for Perseus, comparing SCUBA 850 μm cores with and without internal luminosity sources, as determined using

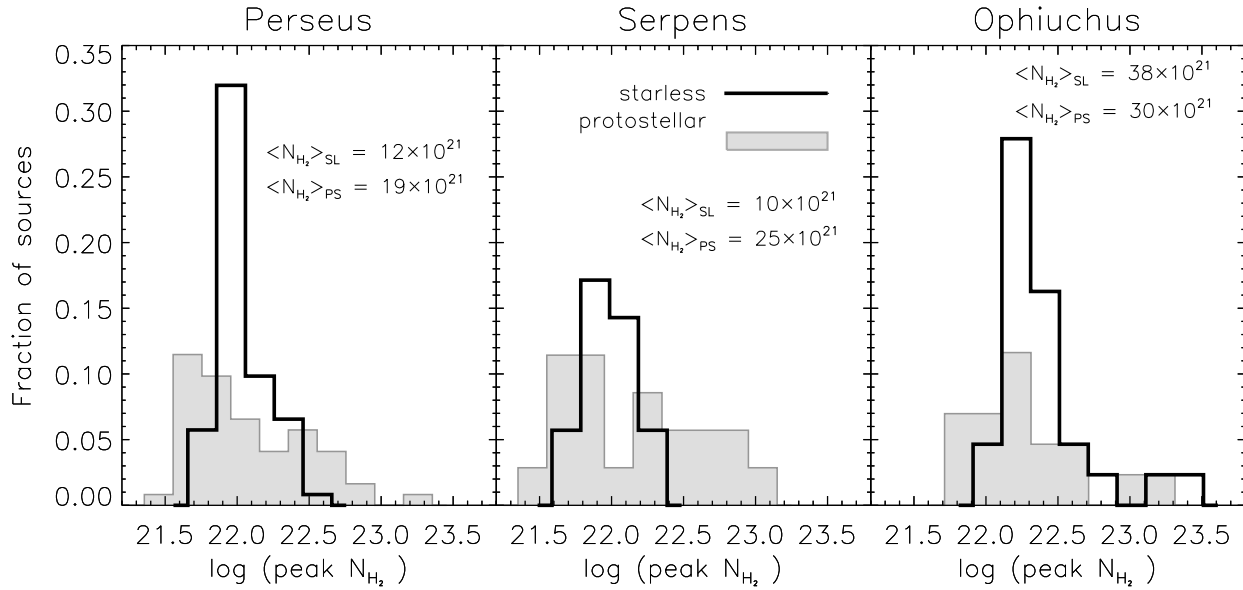


FIG. 6.— Distributions of the peak column density N_{H_2} of starless and protostellar cores. The peak N_{H_2} values of starless cores are considerably lower than those of protostellar cores in both Perseus and Serpens, by factors of approximately 1.6 and 2.5, respectively. In Ophiuchus there is no significant difference in the mean values, but in all three clouds the starless distribution is confined to a narrowly peaked distribution.

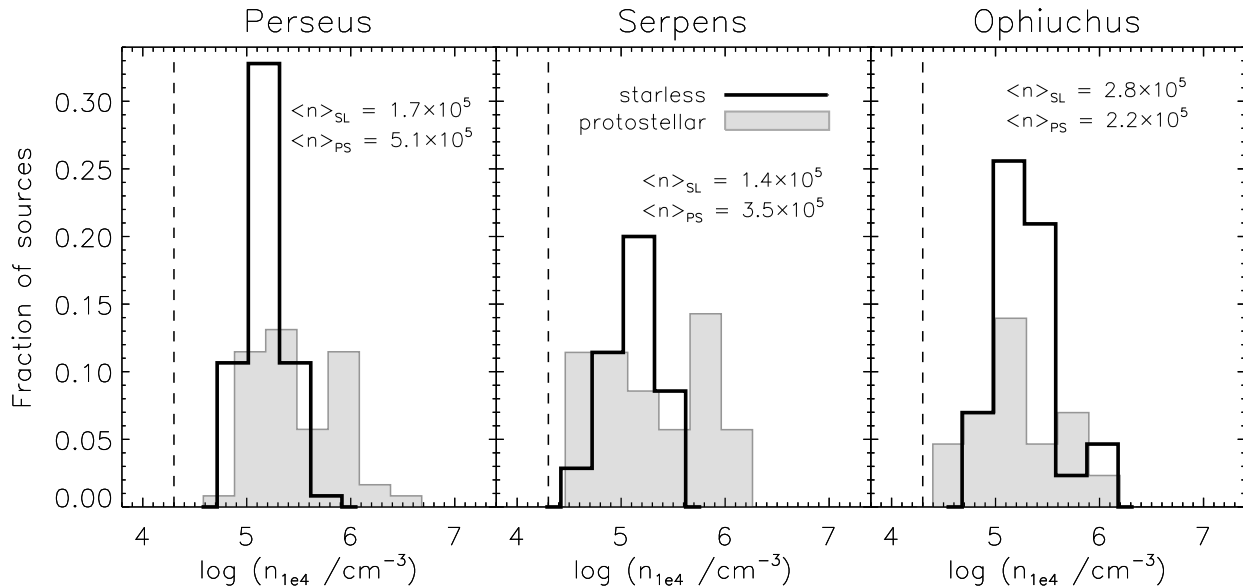


FIG. 7.— Distributions of the mean density n_{1e4} of starless and protostellar cores, where the density is calculated in a fixed linear aperture of diameter 10^4 AU (§ 3.2). As for the peak N_{H_2} distribution (Figure 6), starless cores tend to have lower mean densities than protostellar cores in Perseus and Serpens, by approximately a factor of three. In Ophiuchus, by contrast, there is almost no difference between the two distributions. Note that the Bolocam surveys are only sensitive to relatively dense cores with $n \gtrsim 2 \times 10^4 \text{ cm}^{-3}$ (dashed lines, see Paper III).

Spitzer c2d data. Those authors concluded that cores with embedded YSOs (located within $15''$ of the core position) have higher “concentrations” on average. Note that average n_{1e4} values are much larger than the minimum detectable density of $\sim 2 \times 10^4 \text{ cm}^{-3}$ from Paper III, due in part to few sources near the detection limit and in part to the difference in calculating densities in a fixed aperture.

Density distributions for starless and protostellar cores in Serpens are similar to those in Perseus. Peak N_{H_2} values are substantially smaller for starless ($\langle N_{H_2} \rangle = 10 \times 10^{21} \text{ cm}^{-2}$) than for protostellar ($\langle N_{H_2} \rangle = 25 \times 10^{21} \text{ cm}^{-2}$; Student’s T-test significance 0.04) cores, and form a much narrower distribution. Likewise, typical mean densities of starless cores ($1.4 \times 10^5 \text{ cm}^{-3}$) are nearly three times smaller than those of protostellar cores ($3.5 \times 10^5 \text{ cm}^{-3}$; Student’s T-test significance 0.03). In contrast to Perseus, however, mean density differences in Serpens are due entirely to the higher masses of protostellar cores, as starless and protostellar cores have similar sizes in Serpens. As was the case for core sizes and shapes, there is essentially no difference between the peak or mean densities of starless and protostellar cores in Ophiuchus. Average peak N_{H_2} values are similar ($30 - 40 \times 10^{21} \text{ cm}^{-2}$) and the two distributions have similar dispersions, and average n_{1e4} values are $2.2 - 2.8 \times 10^5 \text{ cm}^{-3}$.

To summarize, peak column densities and mean densities of starless cores in Perseus and Serpens are lower on average than for protostellar cores, whereas in Ophiuchus there is no significant difference between the starless and protostellar populations. The N_{H_2} distributions for starless cores are quite narrow in all three clouds, indicating a small range of column densities. This narrow distribution more likely represents an upper limit to N_{H_2} for starless cores, as we are not sensitive to very large low mass cores (see § 3.3), but in general cores with the highest column densities tend to be protostellar.

3.3. The Mass versus Size Distribution

Figure 8 plots total core mass versus angular FWHM size for starless and protostellar cores in Perseus. The beam size and empirical 50% and 90% completeness limits as a function of size, derived from Monte Carlo simulations (Paper I), are indicated. Completeness limits are lower for protostellar cores by a factor of two due to the higher dust temperature assumed in the mass calculation (15 K) compared to starless cores (10 K). There is approximately a factor of 1.2 increase in mass between the 50% and 90% completeness curves, which holds true for the other clouds as well.

In this diagram, starless cores seem to follow a constant surface density ($M \propto R^2$) curve, consistent with the narrow distribution of peak column densities (Figure 6). Protostellar cores, in contrast, have a narrower range of sizes for a somewhat larger range of masses. This is a restatement of the results from § 3.1 and § 3.2: protostellar cores in Perseus are smaller and have higher mean densities than starless cores. Note that because our completeness limits are similar to $M \propto R^2$, the distribution of starless cores in mass and size only implies that the upper envelope of cores follows a constant surface density curve. For example, there could be a population

of large, low mass cores that we are unable to detect. Nevertheless, the two populations seem to fill different regions of the mass versus size parameter space.

Examining Figure 8, it is easy to imagine how protostellar cores in Perseus might have evolved from the current population of starless cores, by decreasing in size and increasing in density for a constant mass, until collapse and protostellar formation is triggered. Equivalently, the formation of a central protostar within a previously starless core is associated with a decrease in core size and an increase in core density.

Such a simple scenario is not consistent with the other clouds, however, as is evident in Figure 9. Although protostellar cores in Serpens have a small range in sizes for a large range of masses, as seen in Perseus, there is no population of large starless cores in Serpens. In fact, it is unclear how the relatively massive protostellar cores ($\langle M \rangle_{\text{PS}} = 2.1$) in Serpens could have evolved from the current population of compact, low mass starless cores ($\langle M \rangle_{\text{SL}} = 0.9$). It appears that Serpens has exhausted its reserve of starless cores with $M \gtrsim 2M_{\odot}$; unless new cores are formed from the lower density medium, future star formation in the cloud will result in stars of considerably lower mass than the current protostellar population.

This deficit of starless cores at higher core masses may be the result of a mass dependence in the timescale for protostellar formation, with higher mass cores forming protostars more quickly (Hatchell et al. 2008). In both Serpens and Perseus the most massive cores tend to be protostellar in nature, although the trend is much more extreme in Serpens. In Ophiuchus, where core masses are lower on average than in the other clouds, no such distinction between starless and protostellar cores is seen. There is essentially no difference between the starless and protostellar populations in Ophiuchus, suggesting very little core evolution after the formation of a protostar.

3.4. Relationship to Cloud Column Density

We use the cumulative fraction of starless and protostellar cores as a function of cloud A_V , shown in Figure 10, to quantify the relationship between dense cores and the surrounding cloud material. Visual extinction (A_V) is a measure of the cloud column density, and is derived based on the reddening of background 2MASS and IRAC sources, as described in Paper III and Huard et al. (2006). In Paper III, we found that 75% of 1.1 mm cores in Perseus, Serpens, and Ophiuchus are found at visual extinctions of $A_V \gtrsim 8$ mag, $A_V \gtrsim 15$ mag, and $A_V \gtrsim 20 - 23$ mag, respectively. Although these values do not define a strict threshold, below these A_V levels the likelihood of finding an 1.1 mm core is very low. Here we investigate whether the relationship between dense cores and cloud column density is different for starless and protostellar cores.

Figure 10 demonstrates that both starless and protostellar cores are found primarily at high cloud column densities ($A_V > 6$ mag): 75% of starless and protostellar cores in Perseus are located at $A_V \gtrsim 6.5$ and 9.5 mag, respectively, $A_V \gtrsim 8$ and 10 mag in Serpens, and $A_V \gtrsim 19.5$ and 25.5 mag in Ophiuchus. Note that these “threshold” values are significantly higher than the minimum cloud A_V which is approximately 2 mag in Perseus and Ophiuchus, and 6 mag in Serpens. Starless cores tend to be found at somewhat lower A_V than pro-

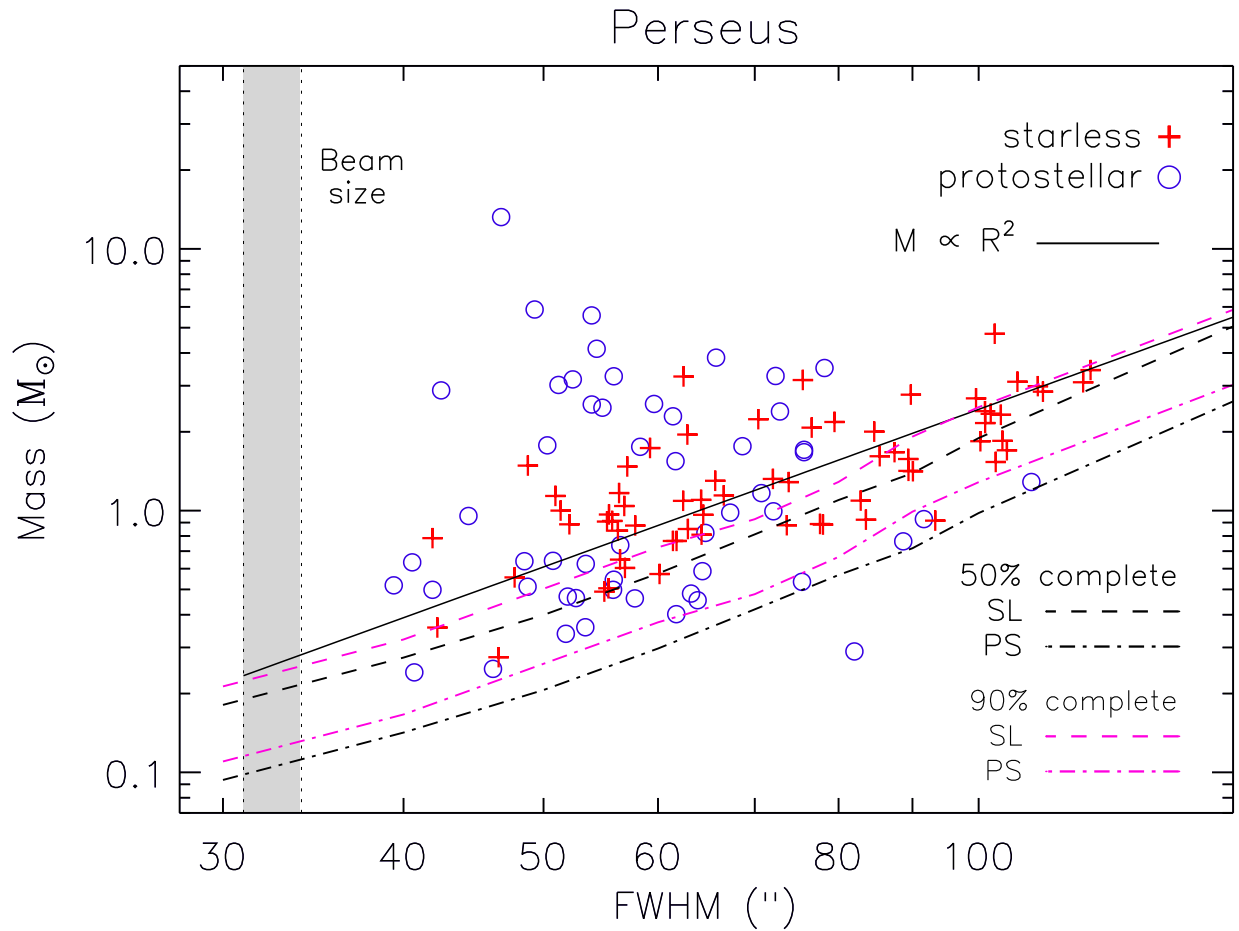


FIG. 8.— Total mass versus angular FWHM size for starless and protostellar cores in Perseus. Dashed and dash-dot lines indicate empirically derived 50% (and 90%; light gray) completeness limits for starless and protostellar cores, respectively. The two populations seem to inhabit different regions of the parameter space: starless cores tend to follow a constant surface density relationship ($M \propto R^2$, solid line), consistent with their narrow distribution in column density (Figure 6), while protostellar cores have a wide range in masses for a relatively small range in sizes. This relationship suggests a simple explanation for how the protostellar cores might have evolved from a similar population of starless cores, with individual cores becoming smaller and denser at a constant mass until protostar formation is triggered.

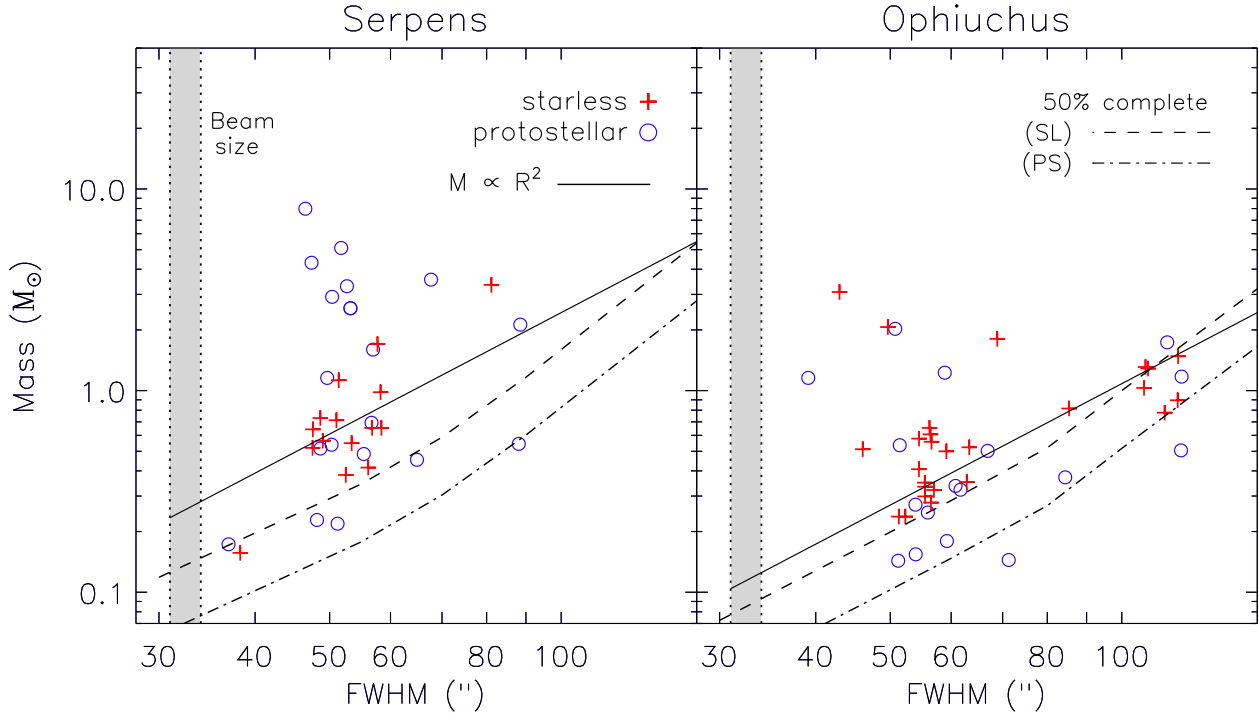


FIG. 9.— Total mass versus angular FWHM size for starless and protostellar cores in Serpens and Ophiuchus. Lines are as in Figure 8; as for Perseus, the 90% completeness curves are approximately a factor of 1.2 higher in mass than the 50% completeness curves, although they are omitted here for clarity. Unlike in Perseus, starless cores do not necessarily follow a constant surface density ($M \propto R^2$) line. Strikingly, there is no population of large starless cores in Serpens; it is not clear how the current population of relatively massive protostellar cores could have evolved from such compact, low mass starless cores. This discrepancy suggests that future star formation in the cloud may result in stars of considerably lower mass than the currently forming protostars.

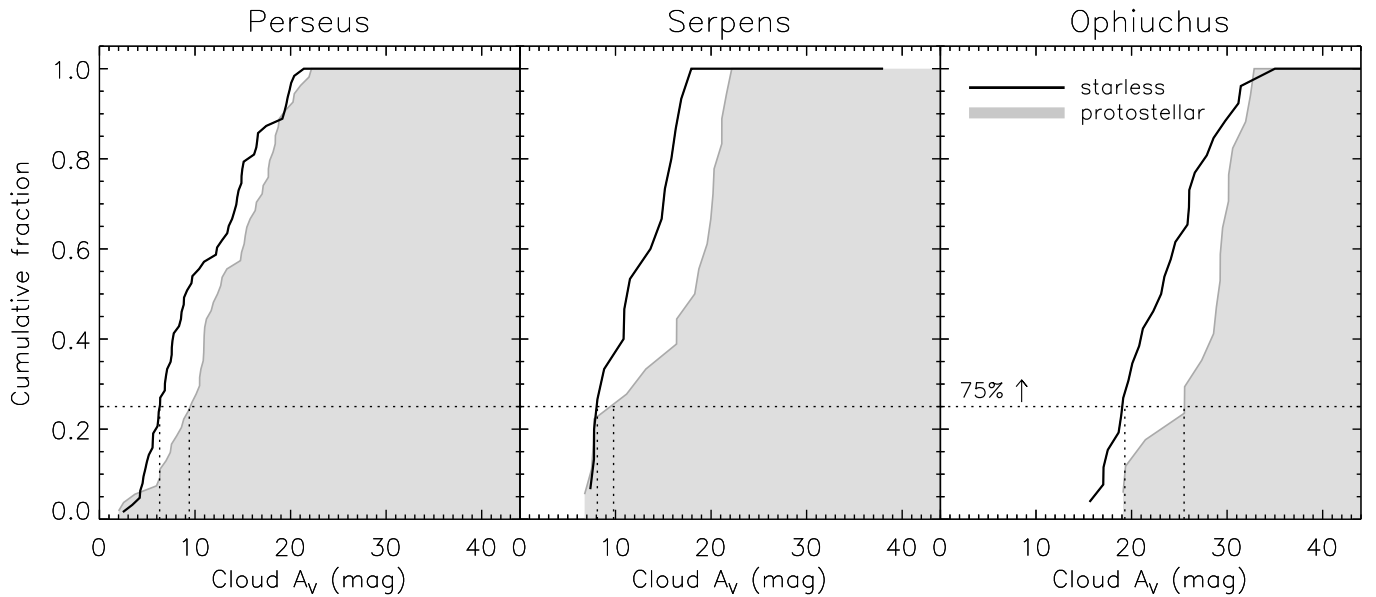


FIG. 10.— Cumulative fraction of starless and protostellar cores as a function of cloud A_V , where the A_V is derived from the reddening of background stars in 2MASS and IRAC data. In all three clouds, the majority of cores are found at high cloud column densities ($A_V > 7$ mag). Dotted lines indicate the A_V at which $> 75\%$ of cores are found; 75% of starless and protostellar cores in Perseus are located at $A_V \gtrsim 6.5$ and 9.5 mag, respectively. The equivalent values are $A_V \gtrsim 6$ and 10 mag in Serpens, and $A_V \gtrsim 19.5$ and 25.5 mag in Ophiuchus. There appears to be a strict extinction threshold in Serpens and Ophiuchus, with no cores found below $A_V \sim 7$ and 15 mag, respectively.

tostellar cores; a two-sided KS test yields probabilities of approximately 1% that the starless and protostellar distributions are drawn from the same parent distribution in each cloud. In Serpens and Ophiuchus there appear to be strict extinction thresholds for 1.1 mm cores at 7 and 15 mag, respectively. A few cores in Perseus and Serpens lie outside the A_V map area, and may be associated with low- A_V material.

As discussed in Paper III, an extinction threshold has been predicted by McKee (1989) for photoionization-regulated star formation in magnetically supported clouds. In this model, core collapse and star formation will occur only in shielded regions of a molecular cloud where $A_V \gtrsim 4 - 8$ mag. The fact that 75% of both protostellar and starless cores are found above $A_V \sim 6$ mag in each cloud is consistent with this model; while it is certainly not the only explanation, magnetic fields may play a role in inhibiting collapse of cores, at least in the low column density regions of molecular clouds.

3.5. Clustering

Finally, we look at the spatial clustering of starless and protostellar cores. The spatial distributions of starless and protostellar cores in each cloud are shown in Figure 3. Starless and protostellar cores appear to cluster together for the most part, often congregating along filamentary structures in the clouds. Both populations occur in the known clusters (e.g. NGC 1333, L 1688) and in a more distributed way across the clouds, with a few exceptions, such as in Perseus where there is a group of primarily starless cores (B1 ridge).

As a more quantitative measure of clustering, we use the two-point correlation function (Figure 11):

$$w(r) = \frac{H_s(r)}{H_r(r)} - 1, \quad (4)$$

where $H_s(r)$ is the number of core pairs with separation between $\log(r)$ and $\log(r + dr)$, and $H_r(r)$ is similar but for a random distribution. The correlation function $w(r)$ is a measure of the excess clustering as compared to a random distribution of sources. The upper panels of Figure 11 plot $w(r)$ as a function of source separation r , with the linear beam size and average source size indicated. The lower panels plot $\log(w)$, with a power law fit ($w(r) \propto r^p$) for r larger than the average source size. In essence, the amplitude of $w(r)$ is a measure of the magnitude of clustering, while the slope is a measure of how quickly clustering falls off on increasing scales.

The amplitude of $w(r)$ is higher for the protostellar samples in all three clouds, indicating that the degree of clustering is stronger on all spatial scales for protostellar cores. Visually, however, starless and protostellar cores tend to cluster in a similar way (Figure 3), and this observation is supported by the similarity in the slope of $w(r)$ for starless and protostellar cores. In Serpens, $p = -1.4 \pm 0.3$ and -1.3 ± 0.6 for the starless and protostellar populations, respectively. The Ophiuchus curves are quite noisy, but the best fit slopes (-1.3 ± 0.3 and -2.2 ± 0.4) are consistent within 2σ . For Perseus the starless correlation function is shallower by 4σ ($p = -1.14 \pm 0.13$ and -1.5 ± 0.1). A shallower slope suggests that, while the amplitude of clustering is weaker for starless cores, it does not fall off as fast at

larger spatial scales.

A lower amplitude of clustering for starless cores as compared to protostellar cores in Perseus and Serpens is confirmed by the peak number of cores per square parsec: 10 pc^{-2} and 16 pc^{-2} , respectively, for starless and protostellar cores in Perseus, and 4 pc^{-2} and 8 pc^{-2} in Serpens. These numbers suggest that clustering in the protostellar samples is a factor of 1.5–2 times stronger than in the starless samples. In Ophiuchus, however, the values of the starless and protostellar populations are identical (12 pc^{-2}).

There are at least three plausible reasons that clustering might be stronger for protostellar cores, two environmental and one evolutionary. The difference may be an environmental effect if cores that are located in regions of the cloud with higher gas density are more likely to collapse to form protostars. In that case, more clustered sources would tend to be protostellar rather than starless. Similarly, if outflows or other protostellar activity trigger the collapse of nearby cores, we would again expect more protostellar sources in clustered regions. If evolution plays a more important role, on the other hand, the spatial distribution of cores might evolve after protostellar formation, for example as a result of dynamical effects.

4. ARE THE STARLESS CORES REALLY PRESTELLAR?

For any discussion of the mass distribution or lifetime of prestellar cores, it is important to determine whether or not our starless cores are likely to be truly prestellar (i.e. will form one or more stars at some point in the future). To this end, we investigate the dynamical state of starless cores by estimating the virial masses of cores in Perseus.

While it is possible that some fraction of the observed starless cores are transient or stable structures that will never form stars, the starless cores detected by our Bolocam surveys have high mean particle densities (typical $n_{1e4} \sim 1 - 3 \times 10^5 \text{ cm}^{-3}$; §3.2), making them likely to be prestellar (Di Francesco et al. 2007; Keto & Caselli 2008). Comparison of our data to molecular line observations is a more robust method of determining if cores are gravitationally bound; line-widths provide a direct estimate of the internal energy of cores, while the 1.1 mm dust masses provide an estimate of the potential energy. An ammonia (NH_3) (J,K)=(1,1) and (2,2) survey of dense cores in Perseus that includes all of the Bolocam-identified 1.1 mm cores has recently been completed by Rosolowsky et al. (2008) at the GBT as part of the COMPLETE project.¹⁰ These observations provide a much-needed measure of the temperature and internal motions of dense millimeter cores.

Figure 12 plots the ratio of the dust mass (M_{dust} , from Tables 4 and 5) to the virial mass (M_{vir}) as a function of M_{dust} for the 70 cores in Perseus that have well-determined line widths and temperatures from (Rosolowsky et al. 2008) NH_3 survey. Although all Bolocam cores were detected in ammonia, not every target had a significant NH_3 (2,2) detection or sufficient signal-to-noise to measure the line width in the presence of the

¹⁰ “The COMPLETE Survey of Star Forming Regions”; <http://cfa-www.harvard.edu/COMPLETE/> (Goodman et al. 2004).

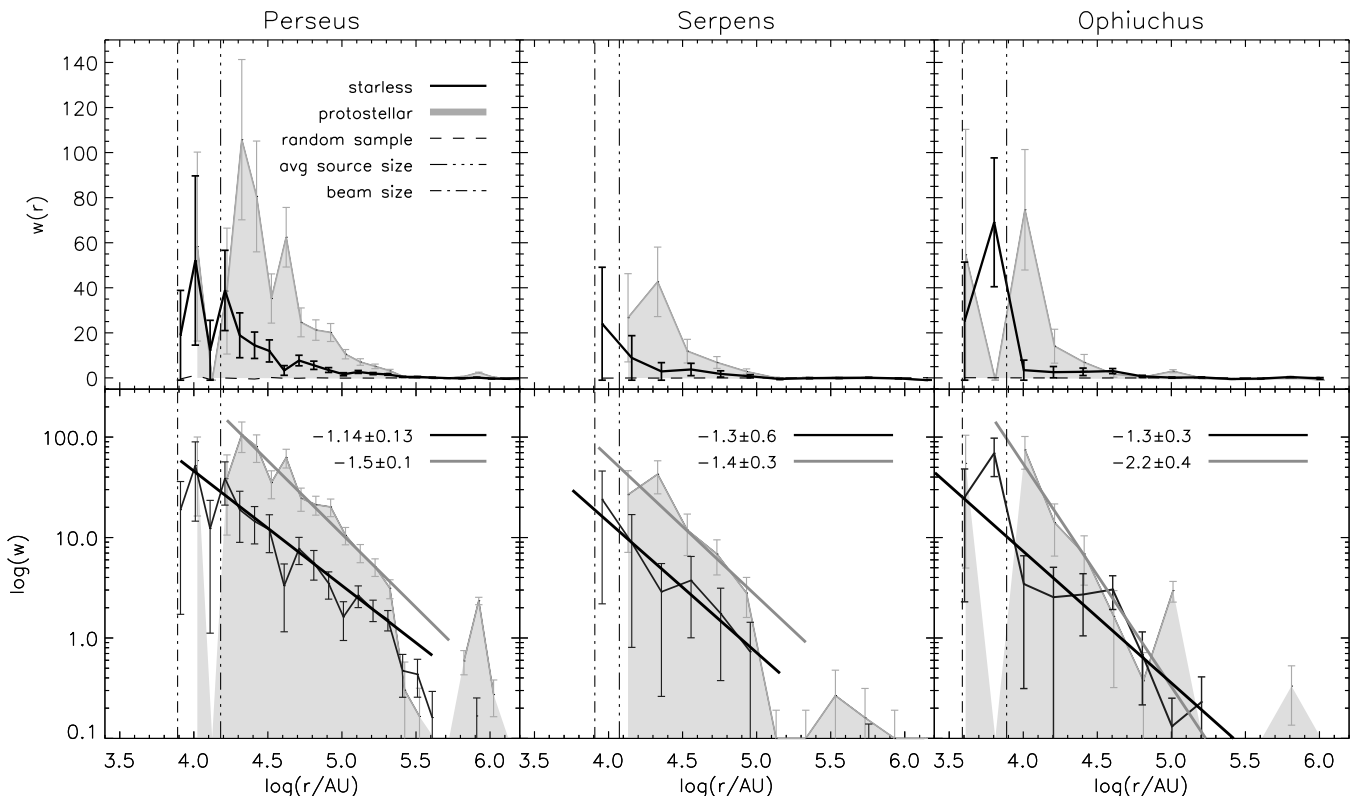


FIG. 11.— Two-point spatial correlation function $w(r)$, plotted as a function of source separation r , for starless and protostellar cores in Perseus, Serpens, and Ophiuchus (upper panels). Lower panels plot $\log(w)$, with the best fitting power law slope for each distribution. Resolution limits and average source sizes are indicated. Power law slopes are fit for r larger than the average source size in each cloud. The amplitude of the protostellar $w(r)$ is consistently higher than the starless $w(r)$, indicating that clustering of protostellar cores is stronger on all spatial scales. Slopes for the starless and protostellar populations are similar in each cloud, however, so although the magnitude of clustering differs, the fundamental nature of the clustering does not.

hyperfine structure. We present the data relevant to Figure 12 in Table 2.

We estimate the virial mass of the cores as

$$M_{\text{vir}} = \frac{5\sigma_{\text{H}_2}^2 R}{aG}, \quad (5)$$

where a accounts for the central concentration of the core, R is the radius of the core, and σ_{H_2} is the line width of the molecular gas inferred from the ammonia line width. Note that $M_{\text{dust}}/M_{\text{vir}} = 1/\alpha$ for $a = 1$, where α is the virial parameter introduced by Bertoldi & McKee (1992). For simplicity, we adopt a power-law density profile, for which $a = (1 - p/3)(1 - 2p/5)^{-1}$. We report values in Table 2 for a $p = 1.5$ profile, giving $a = 5/4$; for $p = 2$ (SIS) the dynamical masses would be 25% smaller. The total line width of H_2 includes thermal and turbulent components, and is calculated as

$$\sigma_{\text{H}_2}^2 = \sigma_{\text{NH}_3}^2 - \frac{kT_K}{17m_{\text{H}}} + \frac{kT_K}{2m_{\text{H}}}. \quad (6)$$

The radius is estimated from the 1.1 mm data as $R = \theta_{\text{dec}}/2$, or the HWHM. Although the effective radius R appropriate for the virial theorem is not exactly equivalent to the gaussian-fit HWHM, we do not expect the correction to be large. If the FWHM is a good representation of $\sqrt{8\ln 2}$ times the radial dispersion one would

measure in the x-y plane for a power law density profile, then we expect

$$R = \theta_{\text{dec}} \sqrt{(5-p)/(3-p)} \sqrt{3/4} \sqrt{1/(8\ln 2)} \quad (7)$$

or $R \sim 0.56 \theta_{\text{dec}}$ for $p = 1.5$, only a 10% correction.

Dotted and solid lines in Figure 12 indicate regions in the plot for which cores should be virialized and self-gravitating, respectively. Note here that $M_{\text{dust}} = M_{\text{vir}}$ implies $2K = -U$, where K is the kinetic and U the gravitational energy, while the self-gravitating limit is defined by $K = -U$, or $M_{\text{dust}}/M_{\text{vir}} = 0.5$. There are two important points to note here. First, nearly all of the starless cores lie close to or above the self-gravitating line, indicating that they are likely to be gravitationally bound. This statement must be modified by the important caveat that the power law profile assumed and the method for measuring the dust mass introduce significant systematics that could shift $M_{\text{dust}}/M_{\text{vir}}$ by more than a factor of two.

Perhaps more convincingly, there is very little difference between starless and protostellar cores in this plot; even though several of the starless cores lie below the self-gravitating line, this region is populated by protostellar cores as well, which are by definition capable of forming stars. Furthermore, recent estimates of the dust opacity $\kappa_{1.1\text{mm}}$ (Shirley et al. 2007; see § 3.2) may increase M_{dust}

TABLE 2
DYNAMICAL PROPERTIES OF PERSEUS CORES

Bolocam ID	T_K (K)	R (10^3 AU)	σ_{H_2} (km s^{-1})	M_{dust} (M_\odot)	M_{vir} (M_\odot)
Per-Bolo 1	9.2	3.8	0.20	0.3	0.7
Per-Bolo 2	9.2	2.0	0.23	0.4	0.4
Per-Bolo 3	10.0	10.7	0.22	0.9	2.4
Per-Bolo 4	10.3	13.1	0.22	2.8	2.9
Per-Bolo 5	12.1	5.9	0.26	2.6	1.7
Per-Bolo 6	9.1	13.2	0.21	3.4	2.5
Per-Bolo 11	11.2	9.1	0.27	1.8	2.9
Per-Bolo 13	9.1	4.8	0.22	1.4	1.1
Per-Bolo 14	9.0	4.8	0.23	1.2	1.1
Per-Bolo 18	11.7	3.2	0.24	0.5	0.8
Per-Bolo 19	10.4	10.4	0.23	1.3	2.5
Per-Bolo 20	10.7	10.1	0.22	1.5	2.3
Per-Bolo 21	11.7	4.9	0.25	0.3	1.5
Per-Bolo 23	11.4	5.7	0.25	0.5	1.6
Per-Bolo 24	11.9	6.9	0.28	0.8	2.5
Per-Bolo 25	10.8	8.9	0.24	0.3	2.3
Per-Bolo 26	10.6	8.2	0.23	1.2	2.0
Per-Bolo 27	10.7	12.9	0.23	1.3	2.9
Per-Bolo 28	10.5	2.8	0.21	0.2	0.5
Per-Bolo 30	10.5	5.3	0.24	0.4	1.3
Per-Bolo 31	11.7	8.1	0.27	2.4	2.7
Per-Bolo 33	10.5	5.8	0.24	0.6	1.5
Per-Bolo 35	11.3	3.8	0.22	0.2	0.8
Per-Bolo 37	13.8	4.1	0.28	0.5	1.5
Per-Bolo 39	14.5	5.4	0.27	0.7	1.7
Per-Bolo 41	12.5	5.0	0.29	0.5	1.9
Per-Bolo 45	12.6	6.6	0.29	2.2	2.4
Per-Bolo 49	14.3	5.5	0.31	2.5	2.3
Per-Bolo 52	11.8	6.7	0.23	1.0	1.6
Per-Bolo 53	13.4	8.5	0.23	1.7	2.0
Per-Bolo 54	13.3	6.3	0.25	1.5	1.7
Per-Bolo 56	9.8	10.5	0.22	1.5	2.3
Per-Bolo 57	10.4	4.4	0.22	0.6	0.9
Per-Bolo 58	10.3	3.2	0.22	0.7	0.7
Per-Bolo 59	10.5	4.8	0.22	0.6	1.1
Per-Bolo 60	11.0	5.7	0.23	0.5	1.3
Per-Bolo 61	10.5	8.6	0.20	0.8	1.6
Per-Bolo 62	10.0	8.0	0.23	1.0	1.9
Per-Bolo 63	10.5	9.9	0.23	1.5	2.4
Per-Bolo 64	9.8	4.6	0.20	0.5	0.8
Per-Bolo 65	11.4	3.7	0.26	1.0	1.2
Per-Bolo 67	10.5	8.0	0.24	1.9	2.0
Per-Bolo 68	9.6	6.3	0.20	0.5	1.2
Per-Bolo 70	10.2	12.2	0.22	4.6	2.7
Per-Bolo 71	11.2	10.4	0.29	2.3	4.1
Per-Bolo 72	10.1	7.7	0.22	2.2	1.7
Per-Bolo 74	10.0	5.6	0.23	0.9	1.3
Per-Bolo 75	9.9	5.6	0.26	0.9	1.7
Per-Bolo 78	9.4	7.9	0.21	1.2	1.6
Per-Bolo 82	9.7	6.0	0.21	0.9	1.2
Per-Bolo 89	12.4	11.9	0.23	1.7	2.7
Per-Bolo 92	9.5	6.3	0.19	0.6	1.1
Per-Bolo 94	9.6	6.6	0.20	0.8	1.2
Per-Bolo 100	12.3	6.7	0.24	1.4	1.7
Per-Bolo 101	14.8	5.6	0.25	0.4	1.6
Per-Bolo 102	11.7	7.5	0.27	1.8	2.5
Per-Bolo 103	12.9	4.9	0.30	3.0	2.0
Per-Bolo 105	12.9	5.8	0.27	1.0	1.9
Per-Bolo 107	11.1	5.8	0.26	1.0	1.7
Per-Bolo 109	10.7	6.6	0.28	0.5	2.4
Per-Bolo 110	10.9	5.7	0.24	0.5	1.5
Per-Bolo 111	10.6	9.7	0.23	1.8	2.3
Per-Bolo 112	12.9	6.7	0.25	0.7	2.0
Per-Bolo 113	10.5	10.7	0.24	0.9	2.7
Per-Bolo 115	10.8	6.6	0.25	1.1	1.9
Per-Bolo 117	10.8	5.4	0.22	0.8	1.2
Per-Bolo 118	10.9	6.6	0.23	0.7	1.6
Per-Bolo 119	10.7	12.7	0.21	2.8	2.5
Per-Bolo 121	10.0	10.4	0.20	1.6	2.0
Per-Bolo 122	11.7	8.5	0.25	1.7	2.4

NOTE. — Kinetic temperatures (T_K) and linewidths (σ_{H_2}) are derived from the NH_3 observations of Perseus cores completed by Rosolowsky et al. (2008). The virial mass M_{vir} is calculated according to Eq. 5, with the effective radius R estimated as the deconvolved HWHM of the 1.1 mm identified core ($\theta_{dec}/2$). M_{dust} is the mass calculated from the total 1.1 mm flux (Tables 4 and 5).

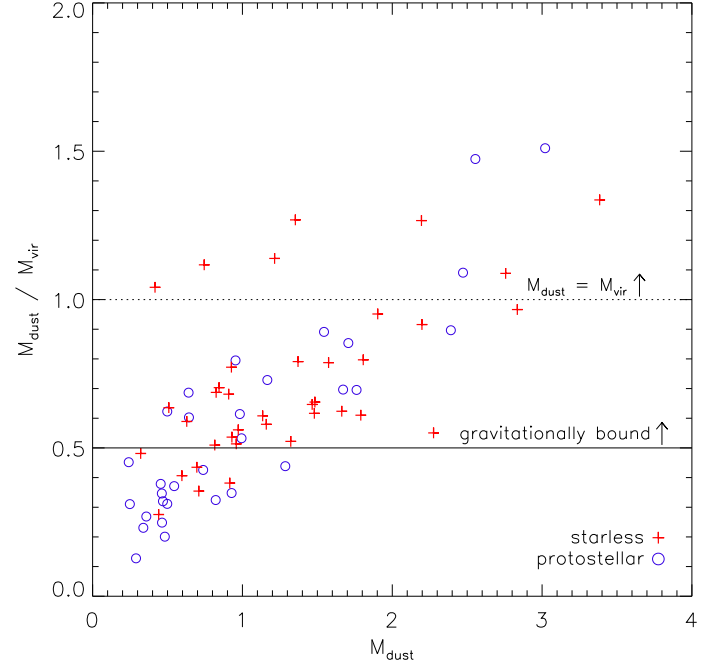


FIG. 12.— Ratio of the total mass derive from dust (M_{dust}) to the virial mass (M_{vir}), calculated using the temperature and velocity dispersion derived from GBT NH_3 (1,1) and (2,2) observations (Rosolowsky et al. 2008), for starless and protostellar cores in Perseus. Only those with well-determined NH_3 line-widths are shown. Solid and dashed lines indicate the minimum M_{dust}/M_{vir} for which cores should be in virial equilibrium (dashed) or self-gravitating (solid).

by 1.3, making the starless cores more bound. Based on this discussion, we assume from here on that all starless cores in our 1.1 mm samples are true prestellar cores.

5. THE PRESTELLAR CORE MASS DISTRIBUTION AND THE IMF

One very important measure of the initial conditions of star formation is the prestellar core mass distribution (CMD). In particular, comparing the prestellar CMD to the stellar initial mass function (IMF) provides insight into how the final masses of stars are determined. There are a number of processes that may (jointly) dictate what the final mass of forming star will be. We focus here on two simple cases, assuming that only one drives the shape of the IMF.

If stellar masses are determined by the initial fragmentation into cores, i.e., the final star or binary mass is always a fixed percentage of the original core mass, then the shape of the emergent stellar IMF should closely trace that of the prestellar CMD (e.g., Myers et al. 1998). This might be expected in crowded regions where the mass reservoir is limited to a protostar's nascent core. If, on the other hand, stellar masses are determined by competitive accretion (Bonnell et al. 2001), or by the protostars themselves through feedback mechanisms (e.g., outflows and winds; Shu et al. 1987), we would not expect the emergent IMF to reflect the original core mass distribution (Adams & Fatuzzo 1996).

5.1. The Prestellar CMD

We combine the prestellar core samples from all three clouds, 108 cores in total, and assume $T_D = 10$ K to calculate masses. As noted above in § 4, our assumption that the majority of starless cores in our sample are truly prestellar is supported by a comparison of the dust mass to the dynamical mass from NH_3 observations. The resulting prestellar CMD is shown in Figure 13.

The 50% completeness limit shown ($M \sim 0.8 M_\odot$; dotted line) is estimated based on the empirical 50% completeness curve in Figure 8. Our completeness depends on the size of a given source; as the average core size in Perseus is $68''$, we take the 50% completeness limit for a $70''$ FWHM source ($M \sim 0.8 M_\odot$) to be the average 50% completeness limit of the sample. The equivalent 90% completeness limit is a factor of 1.2 higher, $M \sim 0.93 M_\odot$. 50% completeness limits for average-sized sources are lower in Serpens ($0.6 M_\odot$) and Ophiuchus ($0.5 M_\odot$), but as more than half of the total population of prestellar cores are in Perseus, we take $0.8 M_\odot$ for the entire prestellar sample.

We fit a power law ($dN/dM \propto M^\alpha$) to the CMD for $M > 0.8 M_\odot$, finding a slope of $\alpha = -2.3$, with a reduced chi-squared of $\tilde{\chi}^2 = 1.9$. The best fit slope depends somewhat on the histogram binning, ranging from 2.0 to 2.6 for bin widths of 0.1 to $0.3 M_\odot$, so we assign a total uncertainty of 0.4 to our best fit slope, when also taking into account formal fitting errors. We fit a lognormal distribution to $M > 0.3 M_\odot$, finding a best-fit width $\sigma = 0.30 \pm 0.03$ and characteristic mass $M_0 = 1.0 \pm 0.1 M_\odot$. Although the lognormal function is quite a good fit ($\tilde{\chi}^2 = 0.5$), the reliability of the turnover in the prestellar CMD is highly questionable given that the completeness limit in Perseus coincides closely with the turnover mass. The prestellar CMD can also be fit by a broken power law with $\alpha = -4.3 \pm 1.1$ for $M > 2.5 M_\odot$ and $\alpha = -1.7 \pm 0.3$ for $M < 2.5 M_\odot$, although the uncertainties are large.

Given that source detection is based on peak intensity, we may be incomplete to sources with very large sizes and low surface density even in the higher mass bins ($M > 0.8 M_\odot$). Completeness varies with size similarly to $M \propto R^2$, thus the fraction of (possibly) missed sources should decrease with increasing mass.¹¹ The effect of missing such low surface brightness cores, if they exist and could be considered prestellar, would be to flatten the CMD slightly (i.e. the true slope would be steeper than the observed slope). Instrumental selection effects are discussed further in Paper I.

To be completely consistent, we should exclude the “unbound” cores from Figure 12 (those with $M_{\text{dust}}/M_{\text{vir}} < 0.5$) from our prestellar CMD. This represents 6 out of the 40 cores that have measured virial masses in Perseus, all 6 of which have $M_{\text{dust}} < 1 M_\odot$. We do not have virial masses for cores in Serpens or Ophiuchus, but we can randomly remove a similar fraction of sources with $M < 1 M_\odot$ from each cloud sample (2 sources from Serpens, 4 from Ophiuchus, and an additional 4 from Perseus). The shaded histogram in Figure 13 indicates how the mass distribution is altered when these 16 “unbound” cores are excluded from the sample. Our derived CMD slope is not affected, as nearly

all of the starless cores below the “gravitationally bound” line in Figure 12 have masses below our completeness limit, and even at low masses the CMD is not significantly changed.

There may also be some concern over the use of a single dust temperature $T_D = 10$ K for all cores. To test the validity of this assumption, we use the kinetic temperatures (T_K) derived from the GBT NH_3 survey of Perseus (Rosolowsky et al. 2008, Schnee et al. 2008, in prep) to compute core masses, assuming that the dust and gas are well coupled (i.e., $T_D = T_K$). Figure 14 shows the CMD of prestellar cores in Perseus, both for a single $T_D = 10$ K, and for masses calculated using the NH_3 kinetic temperatures for each core. There is some change to the shape of the CMD at intermediate masses, but the best-fitting slope for $M > 0.8 M_\odot$ ($\alpha = -2.3$) is unchanged. In fact, the deviation from a power law is smaller when using the kinetic temperatures than when using $T_D = 10$ K ($\tilde{\chi}^2 = 1.3$ and 2.5, respectively).

The median T_K of prestellar cores in Perseus is 10.8 K, quite close to our adopted $T_D = 10$ K, and the small overall shift in masses (a factor of 1.1) corresponding to an 0.8 K temperature difference would not affect the derived CMD slope. The dispersion in kinetic temperatures in Perseus is ± 2.4 K, or $\pm 0.4 M_\odot$ for a $1 M_\odot$ core, and the tail of the distribution extends to $T_K > 15$ K (Schnee et al. 2008, in prep). We do not have temperature information for cores in Serpens or Ophiuchus; if the median temperature were to vary from cloud to cloud by more than a few K, the shape of the combined CMD could be significantly altered. Perhaps a more serious issue is that prestellar cores are not in reality isothermal, but taking into account variations of the temperature with radius requires radiative transfer modeling of each source.

5.2. Comparison to the IMF

The shape of the local IMF is still uncertain (Scalo 2005), but recent work has found evidence for a slope of $\alpha = -2.3$ to -2.8 for stellar masses $M \gtrsim 1 M_\odot$, similar to the slope we measure for the combined prestellar CMD ($\alpha = -2.3 \pm 0.4$). For example, Reid et al. (2002) find $\alpha = -2.5$ above $0.6 M_\odot$, and $\alpha = -2.8$ above $1 M_\odot$. Schröder & Pagel (2003) suggest $\alpha = -2.7$ for $1.1 < M < 1.6 M_\odot$ and $\alpha = -3.1$ for $1.6 < M < 4 M_\odot$. For reference, the Salpeter IMF has a slope of $\alpha = -2.35$ (Salpeter 1955), and the Scalo (1986) slope for sources with mass $M \gtrsim 1 M_\odot$ is $\alpha \sim -2.7$. At lower masses, the IMF flattens, and may be characterized by a lognormal function. Kroupa (2002) suggests a three-component power law for the average single-star IMF: $\alpha = -2.3$ for $0.5 < M < 1 M_\odot$, $\alpha = -1.3$ for $0.08 < M < 0.5 M_\odot$, and $\alpha = -0.3$ for $0.01 < M < 0.08 M_\odot$. Chabrier (2005) finds that a lognormal distribution with $\sigma = 0.55$ and $M_0 = 0.25 M_\odot$ is a good fit for $M < 1 M_\odot$.

The Kroupa (2002) three-component power law and the Chabrier (2005) lognormal IMFs are shown as thick gray lines in Figure 13. The width of the Chabrier (2005) lognormal ($\sigma = 0.55$) is somewhat larger than the width of the prestellar CMD best-fit lognormal ($\sigma = 0.3$), as expected if we are incomplete at lower masses, and the IMF characteristic mass ($M_0 = 0.25 M_\odot$) is a factor of four lower than that of the CMD ($M_0 = 1.0 M_\odot$). A lower characteristic mass for the IMF is expected if some fraction of the core mass is lost in the star-formation

¹¹ Unless $M \propto R^2$ intrinsically for starless cores, in which case a constant incompleteness fraction would apply over all mass bins.

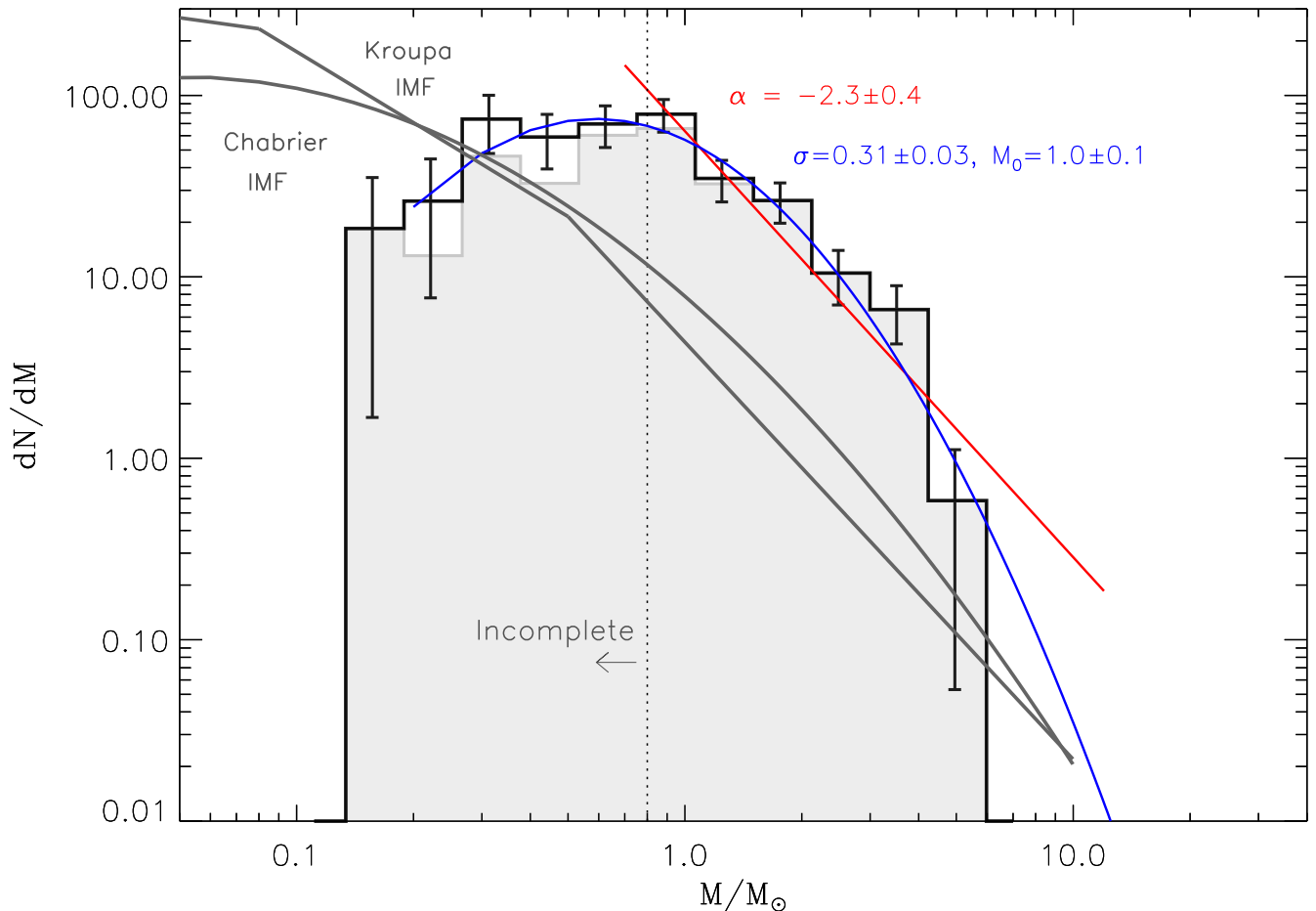


FIG. 13.— Combined prestellar core mass distribution (CMD), with power law and lognormal fits. The prestellar sample is composed of all starless cores from Perseus, Serpens, and Ophiuchus, and the 50% mass completeness limit (dotted line) is defined by the completeness limit for average-sized cores in Perseus. Recent measurements of the stellar IMF for $M \gtrsim 0.5M_{\odot}$ ($\alpha = -2.3$ to -2.8) are similar to the best-fit CMD power law slope ($\alpha = -2.3 \pm 0.4$). IMF fits from Chabrier (2005) (lognormal) and Kroupa (2002) (three-component power law) are shown as thick gray lines for reference. The shaded histogram indicates how the mass distribution changes if a small fraction of cores (15%, based on the six “unbound” cores from Figure 12) with $M < 1M_{\odot}$ are excluded from the prestellar sample.

process. Power law fits for $M > 1 M_{\odot}$ appear to be quite similar for the CMD ($\alpha = -2.3 \pm 0.4$) and IMF ($\alpha = -2.3$ to -2.8), however.

Although we cannot rule out the importance of feedback and other local processes in determining the shape of the IMF, the fact that the prestellar CMD and the local IMF have similar shapes supports a growing body of evidence that the final masses of stars are determined during the core formation process. If this is the case, it is tempting to relate both the prestellar CMD and the IMF to the CMD created from turbulent simulations. Numerical models of turbulent clouds have had some success in reproducing the general shape of the IMF (e.g., Padoan & Nordlund 2002; Li et al. 2004), but the link is not firmly established. For example, we found in Paper III that the predicted dependence of CMD shape on the turbulent mach number (Ballesteros-Paredes et al. 2006; Padoan & Nordlund 2002) does not agree with observations.

Evidence for a direct link between the CMD and the IMF has been found previously based on dust emission surveys of small regions (Testi & Sargent 1998;

Motte et al. 1998), as well as molecular line observations of dense cores (Onishi et al. 2002). Recently, Alves et al. (2007) found evidence for flattening at low masses in the CMD of the Pipe Nebula, as traced by dust extinction toward background stars. Those authors interpret the similarity between the Pipe Nebula CMD and the Trapezium cluster IMF (Muench et al. 2002) as evidence that the stellar IMF is a direct product of the CMD, with a uniform core-to-star efficiency of $30\% \pm 10\%$. Although the measured masses of Alves et al. (2007) are somewhat less uncertain than ours because they do not need to assume a dust opacity or temperature, the mean particle densities of cores traced by dust extinction ($n \sim 5 \times 10^3 - 2 \times 10^4 \text{ cm}^{-3}$) are considerably lower than the mean densities of cores traced by our Bolocam 1.1 mm surveys ($n \sim 2 \times 10^4 - 10^6 \text{ cm}^{-3}$), and they may never form stars. In fact, recent C^{18}O and NH_3 observations suggest that the dust extinction sources in the Pipe Nebula are pressure confined, gravitationally unbound starless cores (Lada et al. 2008; Muench et al. 2007). In Orion, Nutter & Ward-Thompson (2007) find a turnover in the CMD of starless SCUBA $850\mu\text{m}$ cores

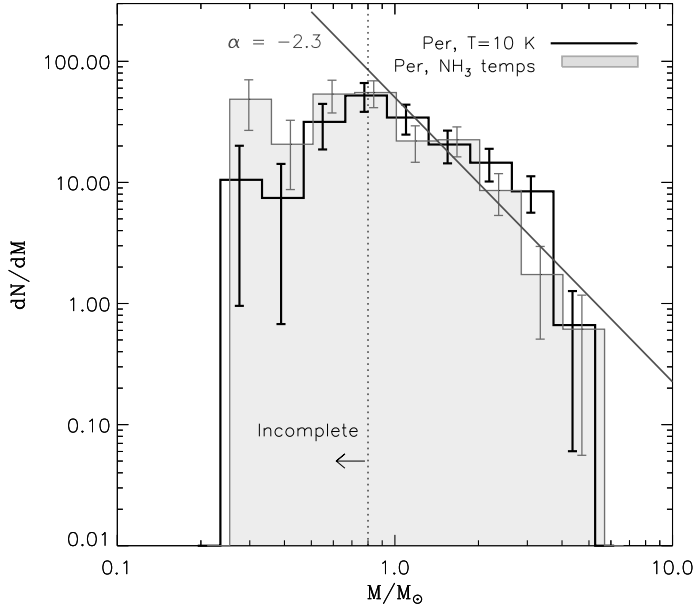


FIG. 14.— Effect on the prestellar CMD in Perseus of using NH_3 -derived core kinetic temperatures (shaded histogram) rather than assuming a constant $T_D = 10\text{K}$ for all cores (black histogram). Only starless cores in Perseus are included here. The best-fitting power-law slope for $M > 0.8M_\odot$ is similar for the two histograms: $\alpha = -2.35 \pm 0.33$ and $\alpha = -2.33 \pm 0.28$ for the $T_D = 10\text{K}$ and NH_3 temperature curves, respectively. Although we do not have kinetic temperatures for cores in Serpens or Ophiuchus, we do not expect temperature effects to dramatically alter the derived prestellar CMD slope.

at $\sim 1.3M_\odot$. Those authors relate this turnover to a down-turn in the Kroupa (2002) IMF at $\sim 0.1M_\odot$, and infer a much lower core-to-star efficiency of $\sim 6\%$.

If the prestellar CMD does have a one-to-one relationship with the stellar IMF, then the ratio of turnover masses is a measure of the core collapse efficiency, or the fraction of original core mass that ends up in the final star: $f_{\text{eff}} = M_{\text{TO}}^{\text{IMF}}/M_{\text{TO}}^{\text{CMD}}$. Here M_{TO} is the mass where the dN/dM distribution, which rises with decreasing mass, flattens out and begins to fall with further decreasing mass. Equivalently, $M_{\text{TO}}^{\text{CMD}}/M_{\text{TO}}^{\text{IMF}} = 1 - f_{\text{eff}}$ is the fraction of core mass lost in the star formation process.

Our limited completeness dictates that we can only measure a lower limit to f_{eff} . If there is a true turnover in the prestellar CMD, it must occur below our completeness limit, at $M_{\text{TO}}^{\text{CMD}} \lesssim 1.0 M_\odot$. The system IMF, i.e., treating binaries and multiple systems as single rather than multiple objects, peaks at $M_{\text{TO}}^{\text{IMF}} \sim 0.2 - 0.3 M_\odot$ (e.g., Chabrier 2005; Luhman et al 2003). This system IMF is appropriate for comparison to our CMDs, as we would not resolve such multiple systems even if they form from distinct cores. For an IMF turnover mass of $0.25 M_\odot$, $M_{\text{TO}}^{\text{CMD}} \lesssim 1.0 M_\odot$ implies that at least 25% of the initial core mass is accreted onto the final star or stellar system. Characteristic masses associated with lognormal fits to both the IMF and CMD imply a similar ratio of $f_{\text{eff}} \gtrsim M_0^{\text{IMF}}/M_0^{\text{CMD}} \sim 0.25/1.0 \sim 0.25$.

Our conclusion that the core-to-star efficiency is at least 25% is consistent with the value found by Alves et al. (2007) for the Pipe Nebula (30%), and

with predicted efficiencies of 25% – 75% from recent analytic models of bipolar protostellar outflows (Matzner & McKee 2000).

5.3. The Effect of “Multiple” Sources

As noted in § 3, 17% – 55% of our protostellar cores are associated with more than one (two to three) embedded protostars. We can expect that a similar fraction of prestellar cores will form a resolved binary or multiple system, making a direct mapping between the CMD and IMF difficult to justify unless the resolutions are matched. Given the relatively low resolution of the Bolocam data ($30''$), some cores must result in wide-separation multiple stellar systems that would not be considered single objects in the system IMF. Furthermore, the system IMF likely evolves over time due to dynamical effects such as the decay of high-order multiples, ejections, and close interactions (see Goodwin et al. 2008, for more discussion of the CMD to IMF mapping).

The effect of these multiple sources will likely be to steepen the CMD, as higher mass cores are divided into multiple lower mass sources. This is consistent with the fact that the prestellar CMD slope is at the low end of the IMF slope range. It is important to keep in mind that we would expect only $\sim 25 - 30\%$ of cores in the combined prestellar CMD to be “multiple” sources, so they should not dominate the CMD slope. While we know that most stars occur in binaries (Duchêne et al. 2007, and references therein), and thus that there must be some unresolved binaries in the *Spitzer* data, these compact systems will most likely be unresolved in the system IMF as well, so they do not affect our comparison.

5.4. The Protostellar Core Mass Distribution

For comparison, we show in Figure 15 the mass distribution of the combined *protostellar* core sample from all three clouds, assuming $T_D = 15\text{K}$. The protostellar CMD is considerably wider and flatter than the prestellar CMD, and extends to higher masses. The best-fitting power law slope ($\alpha = -1.8$; $\chi^2 = 1.7$) is shallower than for the prestellar sample, and the best-fitting lognormal distribution ($\sigma = 0.51 \pm 0.07$, $M_0 = 0.8 \pm 0.2$; $\chi^2 = 1.3$) is wider by nearly a factor of two. The protostellar CMD must be interpreted in the context of a constant assumed $T_D = 15\text{K}$; an intrinsic spread of temperatures would tend to flatten the mass distribution even more, but 15 K has been determined to be the best single T_D based on many detailed radiative transfer models (Shirley et al. 2002; Young et al. 2003).

A protostellar CMD that extends to lower masses than the prestellar CMD is not unexpected, given that some fraction of the core mass has already been accreted on to the central source for protostellar cores. An extension to higher masses in the protostellar CMD as compared to the prestellar CMD, however, can only be explained if (a) we are underestimating the dust temperature of protostellar sources or underestimating the total mass of prestellar cores, (b) the current populations of prestellar cores in these clouds have lower mass than the generation of cores that have already formed protostars, or (c) the highest mass prestellar cores collapse to form protostars very quickly.

Hatchell et al. (2008) examine the relationship between starless and protostellar mass distributions in

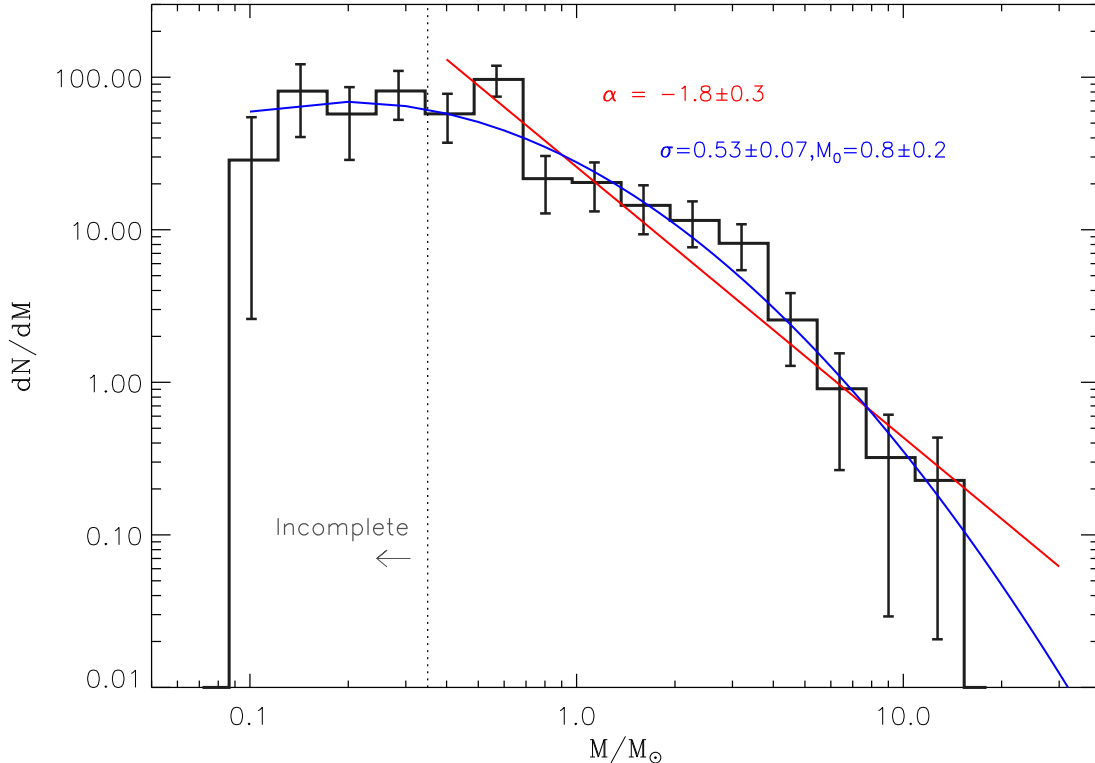


FIG. 15.— Combined protostellar mass distribution, with power law and lognormal fits. The protostellar CMD includes all protostellar cores from Perseus, Serpens, and Ophiuchus, and the 50% mass completeness limit is defined by the completeness to average sized protostellar cores in Perseus. The best-fit power law ($\alpha = -1.8$) is shallower, and the distribution as a whole is wider, than the prestellar CMD (Figure 13). This difference is expected if the protostellar CMD evolved from the prestellar CMD. The fact that the protostellar distribution extends to higher masses than the prestellar CMD is more difficult to explain, however, and may suggest that higher mass prestellar cores are relatively short lived.

Perseus based on SCUBA data, finding that a simple mass-dependent evolutionary model in which higher mass cores form protostars on a shorter timescale than lower mass cores can qualitatively explain the observed steeper prestellar CMD slope, and extension of the protostellar CMD to higher masses. Another step toward resolving the reasons for these differences may be careful radiative transfer models of each prestellar and protostellar source to replace the assumption of a constant T_D .

6. LIFETIME OF THE PRESTELLAR PHASE

We can use the relative number of prestellar cores and embedded protostars to estimate the lifetime of the prestellar core phase, which is essential for understanding the physical processes that govern the formation, support, and collapse of star-forming cores. Several assumptions are required for this calculation. We assume that all of the starless cores in our sample are in fact prestellar, and will eventually collapse to form stars or brown dwarfs (see §4). As we ultimately calibrate our lifetimes based on the Class II phase (2×10^6 yr; Kenyon et al. 1990; Cieza et al. 2007; Spezzi et al. 2008), star formation must have been steady in time for at least the last 2 Myr. In addition, we must assume that there is no significant evolutionary dependence on source mass. Although this kind of analysis relies on a number of assumptions, it has the advantage of being quite simple,

and it does not require on an a priori accretion rate or star-formation model.

Table 3 lists the ratio of the number of starless cores (N_{SL}) to embedded protostars ($N_{\text{emb}} = N_{\text{Class0}} + N_{\text{ClassI}}$) for all three clouds, and the starless core lifetime (t_{SL}) derived from that ratio: $t_{\text{SL}} = t_{\text{emb}}(N_{\text{SL}}/N_{\text{emb}})$. The number of embedded protostars in each cloud is derived in a companion paper (Enoch et al. 2008, in prep), in which the SED derived from c2d *Spitzer* photometry and 1.1 mm fluxes is used to classify protostars based on their bolometric temperature, T_{bol} : Class 0 ($T_{\text{bol}} < 70$ K) and Class I ($70 < T_{\text{bol}} < 650$ K). In addition to the T_{bol} classification, all embedded protostars are required to be detected at 1.1 mm, so that we are complete to embedded sources with $M_{\text{env}} \gtrsim 0.1M_{\odot}$ (Enoch et al. 2008, in prep).

The ratio of the number of starless cores to the number of embedded protostars is $N_{\text{SL}}/N_{\text{emb}} = 1.0$ in Perseus, 0.4 in Serpens, and 0.8 in Ophiuchus. For an embedded protostar phase that lasts $t_{\text{emb}} = 5.4 \times 10^5$ yr (Evans et al. 2008, in prep), the observed ratios imply prestellar core lifetimes of 5×10^5 yr in Perseus, 2×10^5 yr in Serpens, and 5×10^5 yr in Ophiuchus. Note that we also found approximately equal numbers of protostellar and starless cores in all three clouds (Table 1), further confirmation that the lifetime of starless cores is similar to that of the embedded protostellar phase.¹² Therefore,

¹² The $N_{\text{SL}}/N_{\text{emb}}$ ratios in Table 3 differ from $N_{\text{SL}}/N_{\text{PS}}$ in Ta-

TABLE 3
LIFETIME OF THE PRESTELLAR CORE PHASE

Cloud	$N_{\text{SL}}/N_{\text{emb}}$	t_{SL} (yr)	$\langle n_{1e4} \rangle_{\text{SL}}$ (cm^{-3})	t_{ff} (yr)	$t_{\text{SL}}/t_{\text{ff}}$
Perseus	67/66 = 1.0	5×10^5	1.4×10^5	1.4×10^5	3.9
Serpens	15/35 = 0.4	2×10^5	1.2×10^5	1.5×10^5	1.5
Ophiuchus	26/28 = 0.9	5×10^5	1.6×10^5	1.3×10^5	3.9
Combined sample	108/129 = 0.8	4.5×10^5	1.7×10^5	1.4×10^5	3.2
“low density”	78/129 = 0.6	3.3×10^5	1.3×10^5	1.5×10^5	2.2
“high density”	30/129 = 0.2	1.3×10^5	2.8×10^5	1.0×10^5	1.3

NOTE. — N_{emb} refers to the total number of embedded protostars, i.e., those in the Class 0 and Class I phases: $N_{\text{emb}} = N_{\text{Class0}} + N_{\text{ClassI}}$. The number of embedded protostars is derived in a companion paper (Enoch et al. 2008, in prep). The prestellar core lifetime t_{SL} is derived from the number of starless cores: $t_{\text{SL}} = t_{\text{emb}}(N_{\text{SL}}/N_{\text{emb}})$, for an embedded phase lifetime $t_{\text{emb}} = 5.4 \times 10^5$ yr (Evans et al. 2008, in prep). Core mean densities n_{1e4} are calculated in a fixed linear aperture of diameter 10^4 AU, and the free-fall timescale t_{ff} of starless cores is derived from the typical mean density $\langle n_{1e4} \rangle_{\text{SL}}$ of the starless samples using Eq. (8). The “Combined sample” includes sources from all three clouds; this combined sample is divided into “low density” and “high density” bins representing cores with $n_{1e4} < 2 \times 10^5 \text{ cm}^{-3}$ and $n_{1e4} > 2 \times 10^5 \text{ cm}^{-3}$, respectively.

the dense starless cores we are sensitive to last for $2 - 5 \times 10^5$ yr in all three clouds. The differences in $N_{\text{SL}}/N_{\text{emb}}$ from cloud to cloud may be environmental. The ratio is lowest in Serpens, which has the highest mass cores on average. As noted in §5.4, higher mass cores tend to be protostellar, possibly because they collapse on a shorter timescale than lower mass cores.

Taking all three clouds together yields a prestellar core lifetime of 4.5×10^5 yr. The uncertainty in the measured number of prestellar cores is approximately ± 10 , based on the range in the number of starless cores for different identification criteria (see § 2.3). Given a similar uncertainty in the number of embedded protostars (see Enoch et al. 2008, in prep.), this corresponds to an uncertainty in the lifetime of prestellar cores of approximately 0.8×10^5 yr.

Published measurements of the prestellar core lifetime vary by two orders of magnitude, from a few times 10^5 yr to 10^7 yr (Ward-Thompson et al. 2007). For example, Lee & Myers (1999) calculate a core lifetime of 6×10^5 yr for optically selected cores with mean densities of $6 - 8 \times 10^3 \text{ cm}^{-3}$, while Jessop & Ward-Thompson (2000) find a lifetime of 10^7 yr for low density cores detected from column density maps based on IRAS far-infrared observations. Our results are similar to recent findings in Perseus by Jørgensen et al. (2007) and Hatchell et al. (2007), both of whom find approximately equal lifetimes for the starless and embedded protostellar phases by comparing SCUBA 850 μm maps with *Spitzer* c2d data. The approximate equality between N_{SL} and N_{PS} has been found by a number of studies, and was noted early on by Beichman et al. (1986) for the NH_3 cores of Myers & Benson (1983). Our results are also consistent within a factor of two with the lifetime derived by Visser et al. (2002) for a sample of Lynds dark clouds observed with SCUBA.

ble 1 due to the presence of multiple embedded protostars in some protostellar cores (§3) and to the fact that some embedded protostars are “band-filled” at 1.1 mm. Band-filled sources are not associated with a distinct core, but appear to be associated with millimeter emission that is either extended or below the 5σ detection limit.

The average mean density (calculated in a fixed linear aperture of 10^4 AU, see § 3.2) of the starless core samples, $\langle n_{1e4} \rangle_{\text{SL}}$, and corresponding free-fall timescale, t_{ff} , are also given in Table 3. The free-fall time is the timescale on which starless cores will collapse in the absence of internal support, and is calculated from the mean particle density (Spitzer 1978):

$$t_{\text{ff}} = \sqrt{\frac{3\pi}{32G\rho}} = \sqrt{\frac{3\pi}{32G\langle n \rangle \mu_p m_H}}, \quad (8)$$

where m_H is the mass of hydrogen and $\mu_p = 2.33$ is the mean molecular weight per particle. Mean densities are similar in all three clouds, $\langle n_{1e4} \rangle_{\text{SL}} = 1 - 2 \times 10^5 \text{ cm}^{-3}$, with corresponding free-fall times of $t_{\text{ff}} = 1.3 - 1.5 \times 10^5$ yr. The final column in Table 3 gives the ratio of the measured starless core lifetime to the average free-fall timescale in each cloud: $t_{\text{SL}}/t_{\text{ff}} = 1.5 - 3.9$. Thus prestellar cores last for only a few free-fall times in all three clouds.

Such a short prestellar core lifetime argues for a dynamic, rather than quasi-static, core evolutionary scenario. One classical quasi-static model is that of magnetically dominated star formation, in which the evolution of highly sub-critical cores is moderated by ambipolar diffusion (Shu et al. 1987). In this paradigm, prestellar cores should have lifetimes similar to the ambipolar diffusion timescale, or $t_{\text{AD}} \sim 7 \times 10^6$ yr for typical ionization levels in low-mass star forming regions (e.g., Nakano 1998; Evans 1999), more than an order of magnitude longer than our results.

It is important to emphasize here that our Bolocam surveys are sensitive to cores with relatively high mean density ($n \gtrsim 2 - 3 \times 10^4 \text{ cm}^{-3}$; Paper III).¹³ Thus we may be sampling only the densest end stage in a longer core evolutionary picture, in which case a

¹³ Note that this limiting density takes into account the 50% completeness limit to starless cores as discussed in §3.3 and §5.1; it is the typical density found when one calculates a mean density along the 50% completeness curve as a function of size in Figures 8 and 9.

magnetic field dominated scenario could still be applicable at early times (e.g., Tassis & Mouschovias 2004). Ciolek & Basu (2001) also note that t_{AD} can be as short as a few free-fall times for marginally sub-critical cores.

6.1. Density Dependence

Interestingly, if we divide our sample into two density bins, $n_{1e4} < 2 \times 10^5 \text{ cm}^{-3}$ and $n_{1e4} > 2 \times 10^5 \text{ cm}^{-3}$, we find a longer lifetime for lower density cores: 3.3×10^5 yr versus 1.3×10^5 yr for the higher density sample (see Table 3). This result suggests that the prestellar core lifetime becomes shorter as cores become more centrally condensed, at a faster rate than $n^{-0.5}$ (i.e., that expected based on the dependence of t_{ff} on n , see Eq.8). The observed trend, $t_{SL} \propto n^{-1.2}$, is closer to the $n^{-0.85}$ dependence suggested by Jessop & Ward-Thompson (2000).

6.2. Additional Uncertainties

The prestellar lifetime depends on the ratio with protostellar cores, but our sensitivities to prestellar and protostellar sources are not equal due to the different assumed dust temperatures: the protostellar core mass completeness limit is lower by approximately a factor of two. Of the 55 protostellar cores in Perseus, 13 fall between the protostellar and starless completeness limits (similarly 3/20 in Serpens, and 5/17 in Ophiuchus), suggesting that the prestellar core lifetime should perhaps be increased by a factor of 1.3.

We must also consider the possible bias introduced by using the number of embedded protostars, as detected with the higher resolution *Spitzer* data, rather than the number of Bolocam-detected protostellar cores, to calculate the prestellar lifetime. $N_{emb}/N_{PS} = 1.2, 1.8,$ and 1.6 in Per, Ser, and Oph, respectively, as can be seen by comparing Tables 1 and 3. If the starless cores have a similar "multiplicity" fraction that we missing due to the $30''$ resolution of Bolocam, then the prestellar lifetimes would be increased by these factors. If cores fragment at later times, or if multiple protostars collapse from a single core, our lifetimes would not be affected.

On the other hand, if some fraction of the starless core sample are *not* prestellar but unbound starless cores, our calculated lifetime of 4.5×10^5 yr would be an overestimate of the true prestellar core lifetime. Extrapolating from the six cores with $M_{dust}/M_{vir} < 0.5$ in Figure 12, the lifetime could *decrease* by a factor of 1.2. Likewise, the assumed embedded phase lifetime is based on the ratio of Class 0 and Class I protostars to Class II sources; if a large fraction of the Class I source from Evans et al. (2008, in prep) are not embedded protostars but edge-on T Tauri disks (e.g. Crapsi et al. 2008), the embedded phase lifetime could be as low as 2.8×10^5 yr, decreasing the prestellar core lifetime by a factor of two.

Finally, the assumption of a simple continuous flow of star formation for the last 2 Myr may, of course, be incorrect, but without a detailed star formation rate model (which might be equally incorrect) it is the best we can do. We hope to mitigate errors from variations in the star formation rate by averaging over three clouds. Given the range of possible errors, we do not apply correction factors to the numbers in Table 3, but consider the absolute uncertainty in the prestellar core lifetime to be a factor of two in either direction.

7. CONCLUSIONS

Utilizing large-scale 1.1 mm surveys (Enoch et al. 2006; Young et al. 2006; Enoch et al. 2007) together with *Spitzer* IRAC and MIPS maps from the c2d Legacy program (Evans et al. 2003), we have carried out an unbiased census of prestellar and protostellar cores in the Perseus, Serpens, and Ophiuchus molecular clouds. We identify a total of 108 starless and 92 protostellar cores in the three cloud sample. Based on a comparison of 1.1 mm derived masses to virial masses derived from an NH_3 survey of Perseus cores (Rosolowsky et al. 2008), we conclude that the majority of our starless cores are likely to be gravitationally bound, and thus prestellar.

The spatial distributions of both starless and protostellar cores are similar in these three molecular with varying global properties. In all three clouds both starless and protostellar cores are found only at relatively high cloud column densities: 75% of cores are associated with $A_V \gtrsim 6.5 - 9.5$ mag in Perseus, $A_V \gtrsim 6 - 10$ mag in Serpens, and $A_V \gtrsim 19.5 - 25.5$ mag in Ophiuchus. Spatial clustering of starless cores is similar in nature to protostellar cores but lower in amplitude, based on the two-point spatial correlation function and peak surface density of cores.

Cloud environment does appear to have some effect on the physical properties of starless cores, however, and how they differ from cores that have already formed protostars. Starless cores in Perseus are larger and have lower mean densities than protostellar cores; we suggest a simple scenario by which protostellar cores might have evolved from starless cores in that cloud, becoming smaller and denser at a fixed mass. In Serpens, it appears that future star formation will occur in lower mass cores than those that are currently forming protostars. Meanwhile, in Ophiuchus we see essentially no difference between cores that have formed stars and those that have not. Of the three clouds, Serpens has the highest mean cloud density (measured within the $A_V = 2$ contour; Enoch et al. 2007) and the highest turbulent Mach number (Enoch et al. 2007; J. Pineda, personal communication), which may be related to its low fraction of starless cores ($N_{SL}/N_{emb} = 0.4$ compared to 1.0 in the other clouds) and the fact that the higher mass cores have already formed protostars.

The combined prestellar CMD, which includes 108 prestellar cores from three clouds, has a slope above our completeness limit ($0.8M_{\odot}$) of $\alpha = -2.3 \pm 0.4$. This result is consistent with recent measurements of the stellar initial mass function ($\alpha = -2.3$ to -2.8 ; e.g. Reid et al. 2002; Kroupa 2002), providing further evidence that the final masses of stars are directly linked to the core formation process. We place a lower limit on the core collapse efficiency (the percentage of initial core mass that ends up in the final star) of 25%. A more secure link between the CMD and IMF requires measurement of the CMD down to masses less than $0.2M_{\odot}$ in samples of cores that can be demonstrated to be likely prestellar.

In all three clouds the lifetime of dense prestellar cores is similar to the lifetime of embedded protostars, or $2 - 5 \times 10^5$ yr. The three-cloud average is $4.5 \pm 0.8 \times 10^5$ yr (with an absolute uncertainty of a factor of two), arguing strongly for dynamic core evolution on a few free-fall timescales. Such a short prestellar core lifetime is

inconsistent with highly magnetically sub-critical cores, in which case evolution should occur over an ambipolar diffusion timescale ($t_{AD} \sim 10^7$ yr; Nakano e.g., 1998). Our results suggest, rather, a dynamic core evolutionary scenario, as might be appropriate if turbulence dominates the cloud physics (Mac Low & Klessen 2004), or for near-critical magnetic models (Ciolek & Basu 2001). The observed prestellar core lifetime decreases with increasing mean density, at a rate faster than that expected from the dependence of the free-fall timescale on density.

Although this measurement of the prestellar core lifetime supports a dynamic paradigm over a quasi-static one, the distinction is not clear-cut. Our observations could still be consistent with a quasi-static picture if we are only observing the densest stages ($n > 2 \times 10^4 \text{ cm}^{-3}$) of a longer-scale core evolution. Furthermore, the fact that we observe extinction thresholds for finding dense cores at $A_V \gtrsim 6$ mag may be a hint that magnetic fields become important in the low column density regions of molecular clouds, inhibiting the formation of high-density prestellar cores (and thus star formation). Better

measurements of magnetic field strengths and more detailed comparisons between observations and models will be help to resolve these ambiguities.

The authors are grateful to Jens Kauffman and Jason Kirk for their insightful comments and suggestions, and to the anonymous referee for raising questions and issues that helped to improve this work. Support for this work, part of the Spitzer Legacy Science Program, was provided by NASA through contracts 1224608 and 1230782 issued by the Jet Propulsion Laboratory, California Institute of Technology, under NASA contract 1407. Additional support was provided by NASA through the Spitzer Space Telescope Fellowship Program and obtained from NASA Origins Grant NNG04GG24G to the University of Texas at Austin. Support for the development of Bolocam was provided by NSF grants AST-9980846 and AST-0206158. MLE acknowledges support of a Caltech Moore Fellowship and a Spitzer Space Telescope Postdoctoral Fellowship

REFERENCES

- Adams, F. C., & Fatuzzo, M. 1996, *ApJ*, 464, 256
 André, P., Ward-Thompson, D., & Barsony, M. 1993, *ApJ*, 406, 122
 Alves, J., Lada, C. J., & Lada, E. A. 2001, *Nature*, 409, 159
 Alves, J., Lombardi, M., & Lada, C. J. 2007, *A&A*, 462L, 17
 Ballesteros-Paredes, J., Gazol, A., Kim, J., Klessen, R. S., Jappsen, A.-K., & Tejero, E., 2006, *ApJ*, 637, 384
 Ballesteros-Paredes, J., Klessen, R. S., & Vázquez-Semadeni, E. 2003, *ApJ*, 592, 188
 Beichman, C. A., Myers, P. C., Emerson, J. P., Harris, S., Mathieu, R., Benson, P. J., & Jennings, R. E. 1986, *ApJ*, 307, 337
 Bertoldi, F. & McKee, C. F. 1992, *ApJ*, 395, 140
 Bonnell, I. A., Bate, M. R., Clarke, C. J., & Pringle, J. E. 2001, 323, 785
 Bonnor, W. B. 1956, *MNRAS*, 116, 351
 Boss, A., P. & Yorke, H. W. 1995, *ApJ*, 439, L55
 Chabrier, G. 2005 in *The Stellar Initial Mass Function Fifty Years Later*, editors E. Corbelli, F. Palla, and H. Zinnecker, p. 41
 Cieza, L., et al. 2007, *ApJ*, 667, 308
 Ciolek, G. E., & Basu, S. 2001, *ApJ*, 547, 272
 Crapsi, A., van Dishoeck, E. F., Hogerheijde, M. R., Pontoppidan, K. M., & Dullemond, C. P. 2008, *A&A*, in press
 Crutcher, R. M. 1999, *ApJ*, 520, 706
 Di Francesco, J., Evans, N. J., II, Caselli, P., Myers, P. C., Shirley, Y., Aikawa, Y., & Tafalla, M. 2007, in *Protostars and Planets V*, eds. B. Reipurth, D. Jewitt, and K. Keil, p. 17
 Duchêne, G., Delgado Donate, E., Haisch, K. E. Jr., Loinard, L., & Rodriguez, L. F. 2007, in *Protostars and Planets V*, eds. B. Reipurth, D. Jewitt & K. Keil, p. 379
 Ebert, R. 1955, *Zeitschrift Astrophysics*, 37, 217
 Enoch, M. L., Young, K. E., Glenn, J., Evans, N. J., II, Golwala, S., Sargent, A. I., Harvey, P., et al. 2006, *ApJ*, 638, 293
 Enoch, M. L., Glenn, J., Evans, N. J., II, Sargent, A. I., Young, K. E., & Huard, T. L., *ApJ*, in press
 Evans, N. J., II 1999, *ARA&A*, 37, 311
 Evans, N. J., II, Allen, L. E., Blake, G. A., Boogert, A. C. A., Bourke, T., Harvey, P. M., Kessler, J. E., et al. 2003, *PASP*, 115, 965
 Evans, N. J., II, Rawlings, J. M. C., Shirley, Y. L., & Mundy, L. G. 2001, *ApJ*, 557, 193
 Evans, N. J., II, et al. 2007, *Final Delivery of Data from the c2d Legacy Project: IRAC and MIPS*
 Frerking, M. A., Langer, W. D., & Wilson, R. W. 1982, *ApJ*, 262, 590
 Goodman, A. A., & the COMPLETE Team, 2004, in *Star Formation in the Interstellar Medium* (San Francisco: ASP)
 Goodwin, S. P., Nutter, D., Kroupa, P., Ward-Thompson, D., & Whitworth, A. P. 2008, *A&A*, 477, 823
 Gregersen, E. M. & Evans, N. J., II 2000, *ApJ*, 538, 260
 Harvey, P. M., Chapman, N., Lai, S.-P., Evans, N. J., II, Allen, L. E., Jørgensen, J. K., Mundy, L. G., et al. 2006, *ApJ*, 644, 307
 Harvey, P. M., Rebull, L. M., Brooke, T., Spiesman, W. J., Chapman, N., Huard, T. L., Evans, N. J., II, et al. 2007a, *ApJ*, 663, 1139
 Harvey, P. M., Merin, B., Huard, T. L., Rebull, L. M., Chapman, N., Evans, N. J., II, & Myers, P. C. 2007b, *ApJ*, 663, 1149
 Hatchell, J., Fuller, G. A., Richer, J. S., Harries, T. J., & Ladd, E. F. 2007, *A&A*, 468, 1009
 Hatchell, J., & Fuller, G. 2008, *A&A*, in press (preprint: arXiv:0803.1064 [astro-ph])
 Huard, T. L., Myers, P. C., Murphy, D. C., Crews, L. J., Lada, C. J., Bourke, T. L., Crapsi, A., Evans, N. J., II, McCarthy, D. W., Jr., & Kulesa, C. 2006, *ApJ*, 640, 391
 Jessop, N. E., & Ward-Thompson, D. 2000, *MNRAS*, 311, 63
 Johnstone, D., Wilson, C. D., Moriarty-Schieven, G., Joncas, G., Smith, G., Gregersen, E., & Fich, M. 2000, *ApJ*, 545, 327
 Jørgensen, J. K., Harvey, P. M., Evans, N. J., II, Huard, T. L., Allen, L. E., Porras, A., Blake, G. A., et al. 2006, *ApJ*, 645, 1246
 Jørgensen, J. K., Johnstone, D., Kirk, H., & Myers, P. C. 2007, *ApJ*, 656, 293
 Keto, E. & Caselli, P. 2008, *ApJ*, in press (preprint: arXiv:0804.0822 [astro-ph])
 Kenyon, S. J., Hartmann, L. W., Strom, K. M., & Strom, S. E. 1990, *AJ*, 99, 869
 Kroupa, P. 2002, *Science*, 295, 82
 Lada, C. J., & Lada, E. A. 2003, *ARA&A*, 41, 57
 Lada, C. J., Muench, A. A., Rathborne, J., Alves, J. F., & Lombardi, M. 2008, *ApJ*, 672, 410L
 Lada, C. J. & Wilking, B. A. 1984, *ApJ*, 287, 610
 Lee, W. C., & Myers, P. C. 1999, *ApJS*, 123, 233
 Li, P. S., Norman, M. L., Mac Low, M., & Heitsch, F. 2004, *ApJ*, 605, 800
 Luhman, K. L., Stauffer, J. R., Muench, A. A., Reike, G. H., Lada, E. A., Bouvier, J., & Lada, C. J. 2003, *ApJ*, 593, 1115
 Mac Low, M.-M., & Klessen, R. S. 2004, *RevPhys*, 76, 125
 Matzner, C. D., & McKee, C. F. 2000, *ApJ*, 545, 364
 McKee, C. F. 1989, *ApJ*, 345, 782
 McKee, C. F., & Zweibel, E. G. 1992, *ApJ*, 399, 551
 Motte, F., André, P., & Neri, R. 1998, *A&A*, 336, 150
 Meyer, M. R., Adams, F. C., Hillenbrand, L. A., Carpenter, J. M., & Larson, R. B. 2000, in *Protostars and Planets IV*, editors V. Mannings, A. P. Boss, & S. S. Russell, p. 121
 Muench, A. A., Lada, E. A., Lada, C. J., & Alves, J. 2002, *ApJ*, 573, 366
 Muench, A. A., Lada, C. J., & Rathborne, J. M. 2007, *ApJ*, 671, 1820

- Myers, P. C., Adams, F. C., Chen, H., Schaff, E. 1998, *ApJ*, 492, 703
- Myers, P. C., & Benson, P. J. 1983, *ApJ*, 266, 309
- Nakano, T. 1998, *ApJ*, 494, 587
- Nutter, D., & Ward-Thompson, D. 2007, *MNRAS*, 374, 1413
- Onishi, T., Kawamura, A., Tachihara, K., & Fukui, Y. 2002, *ApJ*, 575, 950
- Ossenkopf, V., & Henning, Th. 1994, *A&A*, 291, 943
- Padgett, D. L., et al. 2007, *ApJ*, in press
- Padoan, P., & Nordlund, Å. 2002, *ApJ*, 576, 870
- Rebull, L. M., et al. 2007, *ApJS*, 171, 447
- Reid, I. N., Gizis, J. E., & Hawley, S. L. 2002, *AJ*, 124, 2721
- Rosolowsky, E. W., Pineda, J. E., Foster, J. B., Borkin, M. A., Kauffmann, J., Caselli, P., Myers, P. C., & Goodman, A. A. 2008, *ApJS*, 175, in press
- Salpeter, E. E. 1955, *ApJ*, 121, 161
- Scalo, J. M. 1986, *Fundam. Cosmic Phys.*, 11, 1
- Scalo, J. M. 2005, in *The Stellar Initial Mass Function Fifty Years Later*, Kluwer Academic Publishers, editors E. Corbelli, F. Palla, and H. Zinnecker, p. 23
- Schröder, K.-P., & Pagel, B. E. J. 2003, *MNRAS*, 343, 1231
- Shirley, Y. L., Evans, N. J., II, & Rawlings, J. M. C. 2002, *ApJ*, 575, 337
- Shirley, Y. L., Evans, N. J., II, Rawlings, J. M. C., & Gregersen, E. M. 2000, *ApJS*, 131, 249
- Shirley, Y. L., Huard, T. L., Pontoppidan, K. M., Wilner, D. J., Stutz, A. M., Bieging, J. H., & Evans, N. J., II 2007, *ApJ*, submitted
- Shu, F. H. 1977, *ApJ*, 214, 488
- Shu, F. H., Adams, F. C., & Lizano, S. 1987, *ARA&A*, 25, 23
- Spezzi, L., et al. 2008, *ApJ*, submitted
- Spitzer, L. Jr. 1978, *Physical Processes in the Interstellar Medium*, p. 282
- Tassis, K. & Mouschovias, T. Ch. 2004, *ApJ*, 616, 283
- Testi, L., & Sargent, A. I. 1998, *ApJ*, 508, L91
- Visser, A. E., Richer, J. S., & Chandler, C. J. 2002, *AJ*, 124, 2756
- Ward-Thompson, D., André, P., Crutcher, R., Johnstone, D., Onishi, T., & Wilson, C. 2007, in *Protostars and Planets V*, editors B. Reipurth, D. Jewitt, and K. Keil, p. 33
- Ward-Thompson, D., Scott, P. F., Hills, R. E., & Andre, P. 1994, *MNRAS*, 268, 276
- Young, C. H., Shirley, Y. L., Evans, N. J., II, & Rawlings, J. M. C. 2003, *ApJS*, 145, 111
- Young, K. E., Enoch, M. L., Evans, N. J., II, Glenn, J., Sargent, A., Huard, T. L., Aguirre, J., et al. 2006, *ApJ*, 644, 326

TABLE 4
STARLESS CORES IN PERSEUS, SERPENS, AND OPHIUCHUS

Bolocam ID	RA (hr)	Dec (deg)	Peak flux (mJy/beam)	Total mass (M_{\odot})	θ_{dec} (arcsec)	Axis ratio	n_{1e4} (cm^{-3})
Perseus							
Per-Bolo 1	03 25 07.8	+30 24 22	109	0.28	30.4	1.5	0.9×10^5
Per-Bolo 2	03 25 09.5	+30 23 51	121	0.36	15.7	1.6	1.1×10^5
Per-Bolo 3	03 25 10.2	+30 44 43	125	0.92	85.5	2.1	1.0×10^5
Per-Bolo 4	03 25 17.0	+30 18 53	149	2.99	104.9	1.2	1.5×10^5
Per-Bolo 6	03 25 26.5	+30 21 50	143	2.85	105.6	1.4	1.3×10^5
Per-Bolo 7	03 25 35.4	+30 13 06	126	2.32	98.1	1.4	1.1×10^5
Per-Bolo 9	03 25 37.2	+30 09 55	113	1.70	98.2	1.9	1.0×10^5
Per-Bolo 11	03 25 46.0	+30 44 10	241	2.18	72.5	1.0	2.2×10^5
Per-Bolo 12	03 25 47.5	+30 12 26	118	2.34	95.6	1.8	1.1×10^5
Per-Bolo 13	03 25 48.8	+30 42 24	407	1.14	38.2	1.3	3.9×10^5
Per-Bolo 14	03 25 50.6	+30 42 01	342	1.00	38.7	1.4	3.5×10^5
Per-Bolo 15	03 25 55.1	+30 41 26	188	0.60	46.6	1.1	1.7×10^5
Per-Bolo 16	03 25 56.2	+30 40 41	154	0.50	44.8	1.1	1.5×10^5
Per-Bolo 17	03 25 58.4	+30 37 13	122	0.88	65.9	1.2	0.9×10^5
Per-Bolo 19	03 27 02.0	+30 15 08	115	1.42	83.3	1.1	1.1×10^5
Per-Bolo 20	03 27 28.8	+30 15 02	114	1.67	80.8	1.4	1.1×10^5
Per-Bolo 26	03 28 32.4	+31 04 43	117	1.28	65.5	1.5	1.2×10^5
Per-Bolo 32	03 28 41.7	+30 31 13	144	1.84	94.8	1.1	1.1×10^5
Per-Bolo 33	03 28 42.6	+31 06 12	173	0.65	46.2	1.1	1.9×10^5
Per-Bolo 34	03 28 45.9	+31 15 20	147	0.56	33.0	1.4	1.3×10^5
Per-Bolo 44	03 29 04.5	+31 18 42	274	1.73	47.0	1.7	2.7×10^5
Per-Bolo 45	03 29 07.7	+31 17 17	455	3.25	52.9	1.3	4.8×10^5
Per-Bolo 50	03 29 14.5	+31 20 30	313	3.15	68.0	1.2	3.2×10^5
Per-Bolo 51	03 29 17.0	+31 12 26	423	1.49	34.7	1.4	3.6×10^5
Per-Bolo 55	03 29 19.4	+31 11 37	184	0.89	40.0	1.3	2.1×10^5
Per-Bolo 56	03 29 22.4	+31 36 24	102	1.41	83.7	1.3	1.0×10^5
Per-Bolo 58	03 29 25.7	+31 28 16	273	0.78	25.9	1.2	1.8×10^5
Per-Bolo 61	03 30 24.0	+30 27 39	106	0.89	68.9	1.8	0.8×10^5
Per-Bolo 63	03 30 45.5	+30 52 34	141	1.61	79.0	1.1	1.5×10^5
Per-Bolo 64	03 30 50.4	+30 49 17	86	0.49	36.5	2.2	0.7×10^5
Per-Bolo 67	03 32 26.9	+30 59 11	165	2.07	64.0	2.7	1.6×10^5
Per-Bolo 69	03 32 39.3	+30 57 29	155	3.09	113.5	1.2	1.2×10^5
Per-Bolo 70	03 32 44.0	+31 00 00	238	4.74	97.2	1.2	2.4×10^5
Per-Bolo 71	03 32 51.2	+31 01 48	184	2.77	83.4	1.3	2.0×10^5
Per-Bolo 72	03 32 57.0	+31 03 21	235	2.23	61.8	1.4	2.3×10^5
Per-Bolo 73	03 33 00.0	+31 20 44	178	2.68	93.9	1.3	1.6×10^5
Per-Bolo 74	03 33 01.9	+31 04 32	255	0.91	44.5	1.2	2.6×10^5
Per-Bolo 75	03 33 04.4	+31 04 59	259	0.91	45.0	1.2	2.6×10^5
Per-Bolo 77	03 33 11.4	+31 17 24	110	0.92	76.6	1.3	0.9×10^5
Per-Bolo 82	03 33 25.1	+31 05 35	147	0.88	47.7	1.1	1.4×10^5
Per-Bolo 83	03 33 25.4	+31 20 07	165	1.14	57.9	1.2	1.5×10^5
Per-Bolo 85	03 33 32.1	+31 20 04	155	0.96	54.9	1.4	1.3×10^5
Per-Bolo 86	03 33 51.1	+31 12 37	131	1.53	96.7	1.7	0.9×10^5
Per-Bolo 87	03 35 21.6	+31 06 55	99	1.09	75.6	1.5	0.9×10^5
Per-Bolo 88	03 40 14.5	+32 01 30	162	3.44	114.4	1.6	1.5×10^5
Per-Bolo 89	03 40 49.3	+31 48 35	151	2.40	95.0	1.6	1.4×10^5
Per-Bolo 91	03 41 19.7	+31 47 28	106	0.88	69.3	1.8	0.9×10^5
Per-Bolo 92	03 41 40.0	+31 58 05	94	0.57	50.3	1.2	0.9×10^5
Per-Bolo 93	03 41 45.1	+31 48 10	118	2.16	95.6	1.2	1.2×10^5
Per-Bolo 94	03 41 45.8	+31 57 22	132	0.77	52.4	1.2	1.1×10^5
Per-Bolo 95	03 42 20.6	+31 44 49	108	1.85	98.5	1.2	0.9×10^5
Per-Bolo 96	03 42 47.1	+31 58 41	148	1.10	55.3	1.2	1.5×10^5
Per-Bolo 97	03 42 52.3	+31 58 12	149	0.85	53.8	1.1	1.6×10^5
Per-Bolo 98	03 42 57.3	+31 57 49	134	0.77	52.1	1.1	1.4×10^5
Per-Bolo 99	03 43 38.3	+32 03 09	164	1.04	46.5	1.2	1.7×10^5
Per-Bolo 100	03 43 44.0	+32 03 10	250	1.95	53.7	1.1	2.8×10^5
Per-Bolo 101	03 43 45.6	+32 01 45	139	0.84	45.0	1.4	1.4×10^5
Per-Bolo 105	03 43 57.8	+32 04 06	283	1.47	46.6	1.3	2.8×10^5
Per-Bolo 107	03 44 02.1	+32 02 34	388	1.17	46.0	1.1	4.1×10^5
Per-Bolo 111	03 44 14.5	+31 58 00	170	2.00	77.7	1.4	1.5×10^5
Per-Bolo 112	03 44 14.8	+32 09 13	127	1.09	53.3	1.1	1.2×10^5
Per-Bolo 114	03 44 22.7	+32 10 01	140	1.32	63.5	1.5	1.3×10^5
Per-Bolo 115	03 44 36.4	+31 58 39	167	1.30	53.0	2.1	1.5×10^5
Per-Bolo 117	03 44 48.8	+32 00 30	150	0.97	42.9	1.6	1.5×10^5
Per-Bolo 118	03 44 56.0	+32 00 31	109	0.81	52.7	1.9	1.0×10^5
Per-Bolo 119	03 45 15.9	+32 04 48	181	3.11	101.0	1.3	1.6×10^5
Per-Bolo 121	03 47 33.5	+32 50 55	136	1.57	83.2	1.1	1.3×10^5

TABLE 4
STARLESS CORES IN PERSEUS, SERPENS, AND OPHIUCHUS

Serpens									
Ser-Bolo 1	18 28 23.1	+00 26 35	95	0.65	46.3	1.2	0.9×10^5		
Ser-Bolo 4	18 28 47.2	+00 50 45	145	0.73	35.3	1.3	1.5×10^5		
Ser-Bolo 5	18 28 48.3	+00 14 52	73	0.42	45.3	1.3	0.6×10^5		
Ser-Bolo 6	18 28 50.8	+00 50 29	115	0.55	41.5	1.3	1.2×10^5		
Ser-Bolo 10	18 28 56.6	+00 19 10	107	0.38	41.2	1.1	1.0×10^5		
Ser-Bolo 11	18 28 57.3	+00 48 07	162	0.52	30.2	1.6	1.6×10^5		
Ser-Bolo 12	18 28 58.4	+00 47 36	172	0.64	32.2	1.5	1.7×10^5		
Ser-Bolo 16	18 29 13.5	+00 32 13	175	0.71	37.5	1.5	1.5×10^5		
Ser-Bolo 18	18 29 19.3	+00 33 29	104	0.65	47.2	1.5	1.0×10^5		
Ser-Bolo 19	18 29 31.5	+00 26 49	279	3.34	74.2	1.2	2.8×10^5		
Ser-Bolo 21	18 29 43.4	+00 36 25	129	0.98	48.0	1.2	1.2×10^5		
Ser-Bolo 30	18 30 02.5	+01 15 25	319	1.13	39.6	1.1	2.9×10^5		
Ser-Bolo 31	18 30 02.8	+01 08 38	214	1.70	45.5	1.6	2.1×10^5		
Ser-Bolo 34	18 30 08.2	+01 13 12	153	0.56	34.3	1.5	1.2×10^5		
Ser-Bolo 35	18 30 14.7	+01 13 53	85	0.16	20.2	2.5	0.4×10^5		
Ophiuchus									
Oph-Bolo 1	16 25 59.1	-24 18 16	261	1.29	102.7	1.5	1.4×10^5		
Oph-Bolo 2	16 26 08.1	-24 20 01	388	0.28	46.2	1.1	2.7×10^5		
Oph-Bolo 3	16 26 09.6	-24 19 16	307	0.35	44.8	1.1	2.0×10^5		
Oph-Bolo 6	16 26 22.9	-24 20 01	274	0.35	53.7	1.1	1.2×10^5		
Oph-Bolo 10	16 26 29.7	-24 24 29	2664	2.07	36.8	1.3	13.7×10^5		
Oph-Bolo 13	16 27 04.3	-24 38 47	233	0.82	78.8	1.3	1.3×10^5		
Oph-Bolo 15	16 27 12.2	-24 29 19	437	0.56	45.8	1.3	2.4×10^5		
Oph-Bolo 16	16 27 15.1	-24 30 13	454	0.65	45.6	1.2	2.9×10^5		
Oph-Bolo 21	16 27 33.1	-24 26 49	527	0.61	46.0	1.1	3.5×10^5		
Oph-Bolo 22	16 27 33.4	-24 25 57	496	0.58	43.7	1.0	3.1×10^5		
Oph-Bolo 23	16 27 36.7	-24 26 36	399	0.41	43.7	1.1	2.3×10^5		
Oph-Bolo 24	16 27 58.3	-24 33 10	291	0.24	40.7	1.2	1.6×10^5		
Oph-Bolo 25	16 28 00.1	-24 33 43	332	0.24	39.3	1.2	1.6×10^5		
Oph-Bolo 27	16 28 32.1	-24 17 43	168	0.90	112.8	1.8	0.9×10^5		
Oph-Bolo 28	16 28 57.7	-24 20 34	281	1.31	102.3	1.1	1.5×10^5		
Oph-Bolo 29	16 31 36.4	-24 00 42	284	0.30	44.9	1.1	1.0×10^5		
Oph-Bolo 31	16 31 40.0	-24 49 58	449	0.33	44.9	1.1	3.0×10^5		
Oph-Bolo 32	16 31 40.4	-24 49 26	445	0.32	46.8	1.0	3.0×10^5		
Oph-Bolo 34	16 31 58.0	-24 57 39	264	0.52	54.2	1.2	1.5×10^5		
Oph-Bolo 37	16 32 27.2	-24 29 15	3813	3.08	27.9	1.1	12.7×10^5		
Oph-Bolo 38	16 32 30.1	-23 55 18	245	0.78	108.8	1.3	1.0×10^5		
Oph-Bolo 39	16 32 33.3	-24 29 41	1032	1.81	60.7	1.1	5.2×10^5		
Oph-Bolo 40	16 32 42.3	-24 31 13	154	0.51	31.2	1.3	0.7×10^5		
Oph-Bolo 41	16 32 44.1	-24 33 22	204	0.50	49.0	1.2	0.7×10^5		
Oph-Bolo 42	16 32 49.2	-23 52 34	281	1.48	113.5	1.5	1.5×10^5		
Oph-Bolo 43	16 34 48.3	-24 37 25	212	1.03	101.7	1.2	1.3×10^5		

NOTE. — Bolocam identification is from Papers I-III. The total mass is calculated from the total flux at 1.1 mm, assuming $T_D = 10$ K. Deconvolved angular FWHM sizes (θ_{dec}) and axis ratios are derived from an elliptical gaussian fit, deconvolved by the $31''$ beam. Mean densities are calculated in a fixed linear aperture of diameter 10^4 AU for each source. Note that the Ophiuchus identifications are different than Tables 1 and 2 of Paper II for Oph-Bolo 35 and above due to an adjustment of the source list, resulting in 43 rather than 44 sources (IDs are shifted by -1 for Oph-Bolo 35 and up).

TABLE 5
 PROTOSTELLAR CORES IN PERSEUS, SERPENS, AND OPHIUCHUS

Bolocam ID	RA (hr)	Dec (deg)	Peak flux (mJy/beam)	Total mass (M_{\odot})	θ_{dec} (arcsec)	Axis ratio	n_{1e4} (cm^{-3})
Perseus							
Per-Bolo 5	03 25 22.2	+30 45 09	727	2.55	47.3	1.8	6.5×10^5
Per-Bolo 8	03 25 35.9	+30 45 17	2241	5.86	36.6	1.2	20.6×10^5
Per-Bolo 10	03 25 38.4	+30 43 58	979	2.54	43.1	1.0	8.5×10^5
Per-Bolo 18	03 26 36.9	+30 15 23	225	0.50	25.9	1.2	1.8×10^5
Per-Bolo 21	03 27 37.5	+30 13 53	164	0.34	39.1	1.4	1.5×10^5
Per-Bolo 22	03 27 39.3	+30 12 53	317	0.51	35.8	1.2	2.9×10^5
Per-Bolo 23	03 27 41.7	+30 12 24	283	0.50	45.2	1.2	2.8×10^5
Per-Bolo 24	03 27 47.9	+30 12 02	220	0.82	54.9	1.5	2.3×10^5
Per-Bolo 25	03 28 32.1	+31 11 09	106	0.29	70.9	2.6	0.8×10^5
Per-Bolo 27	03 28 33.3	+30 19 35	155	1.29	103.2	1.6	1.2×10^5
Per-Bolo 28	03 28 34.0	+31 07 01	137	0.24	22.5	1.3	1.0×10^5
Per-Bolo 29	03 28 36.2	+31 13 26	267	0.52	13.9	1.4	2.5×10^5
Per-Bolo 30	03 28 39.0	+31 05 59	189	0.36	42.3	1.1	2.0×10^5
Per-Bolo 31	03 28 39.9	+31 17 57	385	2.39	64.3	1.5	4.1×10^5
Per-Bolo 35	03 28 48.4	+31 16 02	132	0.25	30.0	1.5	1.2×10^5
Per-Bolo 36	03 28 48.7	+30 43 25	127	0.76	81.0	1.9	0.9×10^5
Per-Bolo 37	03 28 52.1	+31 18 08	157	0.47	32.4	2.1	1.5×10^5
Per-Bolo 38	03 28 55.3	+31 14 32	1224	4.15	42.8	1.3	10.7×10^5
Per-Bolo 39	03 28 55.3	+31 19 18	206	0.74	42.8	1.8	2.0×10^5
Per-Bolo 40	03 29 00.0	+31 21 38	685	1.75	48.2	1.2	6.7×10^5
Per-Bolo 41	03 29 00.6	+31 11 59	190	0.46	40.0	1.4	1.7×10^5
Per-Bolo 42	03 29 01.3	+31 20 33	1079	3.17	40.9	1.1	10.7×10^5
Per-Bolo 43	03 29 02.6	+31 15 57	2157	5.57	42.3	1.3	19.2×10^5
Per-Bolo 46	03 29 08.3	+31 15 11	741	3.27	64.6	1.1	7.8×10^5
Per-Bolo 47	03 29 08.9	+31 21 44	612	3.50	71.0	1.2	6.5×10^5
Per-Bolo 48	03 29 10.9	+31 13 26	5177	13.2	31.4	1.4	42.3×10^5
Per-Bolo 49	03 29 11.3	+31 18 25	835	2.47	44.2	1.1	7.9×10^5
Per-Bolo 52	03 29 17.1	+31 27 39	269	0.98	53.8	2.3	2.2×10^5
Per-Bolo 53	03 29 18.2	+31 25 17	336	1.71	67.5	1.5	3.2×10^5
Per-Bolo 54	03 29 19.1	+31 23 27	330	1.54	50.2	1.7	3.2×10^5
Per-Bolo 57	03 29 22.9	+31 33 17	224	0.64	34.8	1.3	2.1×10^5
Per-Bolo 59	03 29 51.5	+31 39 13	249	0.64	38.5	1.2	2.1×10^5
Per-Bolo 60	03 30 14.9	+30 23 37	125	0.46	45.1	1.7	1.1×10^5
Per-Bolo 62	03 30 32.0	+30 26 19	199	0.99	64.1	1.2	1.9×10^5
Per-Bolo 65	03 31 20.0	+30 45 30	522	0.95	29.7	1.2	4.7×10^5
Per-Bolo 66	03 32 17.3	+30 49 44	1068	2.88	27.2	1.1	9.2×10^5
Per-Bolo 68	03 32 28.1	+31 02 18	110	0.45	50.1	2.2	1.1×10^5
Per-Bolo 76	03 33 11.4	+31 21 31	116	0.53	67.6	1.4	1.1×10^5
Per-Bolo 78	03 33 13.2	+31 19 50	262	1.17	62.7	1.2	2.5×10^5
Per-Bolo 79	03 33 15.0	+31 07 02	605	2.29	52.1	1.1	6.8×10^5
Per-Bolo 80	03 33 17.8	+31 09 30	1083	3.84	56.7	1.3	9.5×10^5
Per-Bolo 81	03 33 20.5	+31 07 37	1222	3.26	45.4	1.1	11.3×10^5
Per-Bolo 84	03 33 26.8	+31 06 50	186	0.59	55.5	1.1	1.8×10^5
Per-Bolo 90	03 41 09.0	+31 44 33	139	0.16	...	1.5	0.9×10^5
Per-Bolo 102	03 43 50.5	+32 03 17	432	1.76	60.2	1.2	4.4×10^5
Per-Bolo 103	03 43 55.9	+32 00 46	994	3.02	39.0	1.2	9.0×10^5
Per-Bolo 104	03 43 57.3	+32 03 04	777	1.78	38.0	1.2	7.4×10^5
Per-Bolo 106	03 44 01.6	+32 02 02	426	0.63	42.4	1.1	4.2×10^5
Per-Bolo 108	03 44 02.3	+32 04 57	139	0.40	51.9	1.4	1.2×10^5
Per-Bolo 109	03 44 05.0	+32 00 28	127	0.48	52.7	1.6	1.1×10^5
Per-Bolo 110	03 44 05.2	+32 02 06	257	0.54	45.4	1.1	3.0×10^5
Per-Bolo 113	03 44 22.6	+31 59 23	122	0.93	85.1	1.5	1.2×10^5
Per-Bolo 116	03 44 43.9	+32 01 25	289	0.63	21.0	1.3	2.7×10^5
Per-Bolo 120	03 45 48.1	+32 24 15	83	0.10	...	1.0	0.5×10^5
Per-Bolo 122	03 47 40.8	+32 51 57	262	1.67	67.7	1.4	2.7×10^5
Serpens							
Ser-Bolo 2	18 28 44.0	+00 53 03	198	0.69	46.1	1.2	1.0×10^5
Ser-Bolo 3	18 28 45.8	+00 51 32	227	0.52	35.3	1.3	1.1×10^5
Ser-Bolo 7	18 28 53.0	+00 19 04	119	0.22	39.0	1.2	0.6×10^5
Ser-Bolo 8	18 28 55.2	+00 29 28	617	3.55	59.2	1.2	3.2×10^5
Ser-Bolo 9	18 28 55.9	+00 48 30	141	0.23	31.9	1.6	0.7×10^5
Ser-Bolo 13	18 29 00.2	+00 30 20	239	0.48	44.7	1.1	1.2×10^5
Ser-Bolo 14	18 29 07.0	+00 30 42	1016	2.92	38.3	1.1	4.8×10^5
Ser-Bolo 15	18 29 09.6	+00 31 37	626	1.16	36.8	1.3	3.0×10^5
Ser-Bolo 17	18 29 16.4	+00 18 15	82	0.54	81.7	1.2	0.4×10^5
Ser-Bolo 20	18 29 31.9	+01 19 01	337	2.12	82.3	1.0	1.7×10^5
Ser-Bolo 22	18 29 48.8	+01 16 51	1694	5.10	39.9	1.2	8.1×10^5

TABLE 5
 PROTOSTELLAR CORES IN PERSEUS, SERPENS, AND OPHIUCHUS

Ser-Bolo 23	18 29 50.2	+01 15 25	3010	7.98	33.2	1.0	13.2×10^5
Ser-Bolo 24	18 29 53.8	+00 36 10	202	0.54	38.0	1.2	1.0×10^5
Ser-Bolo 25	18 29 57.4	+01 13 15	1981	4.31	34.1	1.2	9.5×10^5
Ser-Bolo 26	18 29 59.2	+01 14 07	1331	2.56	41.7	1.2	6.6×10^5
Ser-Bolo 27	18 30 00.3	+01 10 38	425	1.60	45.5	1.5	2.2×10^5
Ser-Bolo 28	18 30 00.7	+01 12 57	1266	2.56	41.7	1.2	6.6×10^5
Ser-Bolo 29	18 30 01.0	+01 11 49	979	3.30	40.9	1.3	4.9×10^5
Ser-Bolo 32	18 30 05.7	+00 39 32	105	0.45	55.8	1.3	0.5×10^5
Ser-Bolo 33	18 30 06.4	+00 42 37	126	0.17	16.7	1.1	0.4×10^5
Ophiuchus							
Oph-Bolo 4	16 26 09.9	-24 20 29	397	0.15	43.0	1.1	1.3×10^5
Oph-Bolo 5	16 26 20.7	-24 22 17	365	0.50	58.5	1.1	1.2×10^5
Oph-Bolo 7	16 26 24.7	-24 21 08	407	0.34	51.2	1.2	1.2×10^5
Oph-Bolo 8	16 26 27.2	-24 22 27	1382	1.23	48.9	1.1	4.4×10^5
Oph-Bolo 9	16 26 27.6	-24 23 37	2696	2.02	38.5	1.2	8.8×10^5
Oph-Bolo 11	16 26 32.6	-24 24 45	1249	0.54	39.8	1.1	4.0×10^5
Oph-Bolo 12	16 27 00.7	-24 34 17	540	1.74	109.8	1.2	1.9×10^5
Oph-Bolo 14	16 27 07.9	-24 36 54	261	0.37	76.9	1.6	0.6×10^5
Oph-Bolo 17	16 27 22.3	-24 27 36	404	0.32	52.2	1.2	1.2×10^5
Oph-Bolo 18	16 27 25.2	-24 40 29	472	1.17	114.6	1.6	1.3×10^5
Oph-Bolo 19	16 27 27.0	-24 26 57	615	0.25	45.5	1.1	2.3×10^5
Oph-Bolo 20	16 27 29.1	-24 27 11	691	0.27	42.9	1.1	2.3×10^5
Oph-Bolo 26	16 28 21.0	-24 36 00	225	0.51	114.8	1.2	0.6×10^5
Oph-Bolo 30	16 31 37.2	-24 01 52	289	0.14	39.0	1.2	0.5×10^5
Oph-Bolo 33	16 31 52.6	-24 58 01	204	0.18	49.3	1.2	0.5×10^5
Oph-Bolo 35	16 32 00.6	-24 56 14	189	0.14	63.3	1.2	0.4×10^5
Oph-Bolo 36	16 32 24.3	-24 28 49	4624	1.16	17.6	1.3	4.7×10^5

NOTE. — Table columns are as for Table 4. Note that the Ophiuchus identifications are different than Tables 1 and 2 of Paper II for Oph-Bolo 35 and above due to an adjustment of the source list, resulting in 43 rather than 44 sources. The peak flux, total mass, sizes, etc. for Oph-Bolo 35 and Oph-Bolo 36 are also different than in Paper II.